NASA/TM–2015-218800

Feasibility of Rayleigh Scattering Flow Diagnostics in the National Transonic Facility

Gregory C. Herring and Joseph W. Lee
Langley Research Center, Hampton, Virginia

William K. Goad
Jacobs Technology, Inc., Hampton, Virginia

September 2015

NASA STI Program . . . in Profile

Since its founding, NASA has been dedicated to the advancement of aeronautics and space science. The NASA scientific and technical information (STI) program plays a key part in helping NASA maintain this important role.

The NASA STI program operates under the auspices of the Agency Chief Information Officer. It collects, organizes, provides for archiving, and disseminates NASA's STI. The NASA STI program provides access to the NTRS Registered and its public interface, the NASA Technical Reports Server, thus providing one of the largest collections of aeronautical and space science STI in the world. Results are published in both non-NASA channels and by NASA in the NASA STI Report Series, which includes the following report types:

- TECHNICAL PUBLICATION. Reports of completed research or a major significant phase of research that present the results of NASA Programs and include extensive data or theoretical analysis. Includes compilations of significant scientific and technical data and information deemed to be of continuing reference value. NASA counter-part of peer-reviewed formal professional papers but has less stringent limitations on manuscript length and extent of graphic presentations.

- TECHNICAL MEMORANDUM. Scientific and technical findings that are preliminary or of specialized interest, e.g., quick release reports, working papers, and bibliographies that contain minimal annotation. Does not contain extensive analysis.

- CONTRACTOR REPORT. Scientific and technical findings by NASA-sponsored contractors and grantees.

- CONFERENCE PUBLICATION. Collected papers from scientific and technical conferences, symposia, seminars, or other meetings sponsored or co-sponsored by NASA.

- SPECIAL PUBLICATION. Scientific, technical, or historical information from NASA programs, projects, and missions, often concerned with subjects having substantial public interest.

- TECHNICAL TRANSLATION. English-language translations of foreign scientific and technical material pertinent to NASA's mission.

Specialized services also include organizing and publishing research results, distributing specialized research announcements and feeds, providing information desk and personal search support, and enabling data exchange services.

For more information about the NASA STI program, see the following:

- Access the NASA STI program home page at http://www.sti.nasa.gov

- E-mail your question to help@sti.nasa.gov

- Phone the NASA STI Information Desk at 757-864-9658

- Write to:
  NASA STI Information Desk
  Mail Stop 148
  NASA Langley Research Center
  Hampton, VA 23681-2199

Feasibility of Rayleigh Scattering Flow Diagnostics in the National Transonic Facility

Gregory C. Herring and Joseph W. Lee
Langley Research Center, Hampton, Virginia

William K. Goad
Jacobs Technology Inc., Hampton, Virginia

Feasibility of Rayleigh Scattering Flow Diagnostics
in the National Transonic Facility

Gregory. C. Herring, Joseph W. Lee, and

NASA Langley Research Center
18 Langley Blvd., Hampton, VA 23681

William K. Goad

Jacobs Technology, Inc.
5 Manhattan Sq., Hampton, VA 23666

Abstract

Laser-based Rayleigh light scattering (RLS) was performed in the National Transonic Facility (NTF) at NASA Langley Research Center. The goal was to determine if the free-stream flow undergoes clustering (early stage of condensation from gas to liquid) or remains in a pure diatomic molecular phase. Data indicate that clusters are not observable down to levels of 10% of the total light scatter for a variety of total pressures at one N_2 cryogenic-mode total temperature (T_t = -50 °F = 227 K) and one air-mode temperature (T_t = +130 °F = 327 K). Thus RLS appears viable as a qualitative or quantitative diagnostic for flow density in NTF in the future.

Particles are distinguished from optically unresolvable clusters because they are much larger and individually resolvable in the laser beam image with Mie scattering. The same RLS apparatus was also used, without modification, to visualize naturally occurring particles entrained in the flow for both cryogenic and air-modes. Estimates of the free-stream particle flux are presented, which may be important for interpretation of laminar-to-turbulent boundary-layer transition studies.

List of Acronyms and Symbols

AoA	Angle of attack
CCD	Charge coupled device
ETW	European Transonic Wind Tunnel
FOV	Field of view
LN2	Liquid Nitrogen
LaRC	Langley Research Center
NPR	Nozzle pressure ratio
NTF	National Transonic Facility
rpm	revolutions per minute
PMT	Photomultiplier tube (a type of optical detector)
RLS	Rayleigh light scattering
SNR	Signal-to-noise ratio
TCT	Transonic Cryogenic Tunnel
UPWT	Unitary Plan Wind Tunnel

---

dm/dt	total mass flow down the test section (kg/s)
D	Molecule, cluster, or particle diameter (m)
E_{beam}	Energy transmitted through laser beam cross section during a fixed observation time (J)
L_{vert}	Distance along laser beam that is imaged onto one camera pixel (m)
M	Mach number = flow speed / sound speed
N	Number density of molecules, clusters, or particles ($1/m^3$)
N_{sig}	Number of photoelectrons generated on detector cathode
P_t	Total pressure (Pa or psi)
P_s	Free-stream static pressure (Pa or psi)
Q	Ratio of measured to calculated Rayleigh scattering signal
R	Reynolds number per unit distance (1/m or 1/ft)
T_{sig}	Fractional transmission of RLS signal light from the sample volume (near the focus of the laser beam) to the photocathode of the detector
T_{beam}	Fractional transmission of light from the laser output to the sample volume
$T_{transit}$	Time for a particle to transit the laser beam diameter (s)
T_t	Total temperature (K or °F or °R)
T_s	Free-stream static temperature (K or °F or °R)

η_{QE}	Quantum efficiency of optical detector photocathode
$\rho_t \propto P_t / T_t$	Total density (kg/m^3)
$\rho_s \propto P_s / T_s$	Free-stream static density (kg/m^3)
λ	Wavelength of incident light that is scattered (m)
Ω	Detection solid angle for optical detector (sr)
$(d\sigma/d\Omega)$	Differential scattering cross section per molecule [or cluster] (m^2/sr)
$(d\sigma/d\Omega)_{90}$	Differential cross section at 90 deg to beam direction (m^2/sr)

I. Introduction

Background

Rayleigh light scattering (RLS) is a nonintrusive technique [1] for wind tunnel diagnostics for either quantitative or qualitative flow density, since the signal is proportional to the product of fluid density and source brightness. This diagnostic became more practical after invention of the laser due to the brightness of laser beams. For measurements at a single spatial point, RLS was limited by Mie scatter of impurity particles that was not easily distinguished from the Rayleigh scatter of the molecular constituent. The advent of the modern digital camera further simplified RLS by allowing convenient imaging of a finite portion of the flow field. In addition to providing significantly more information, the ability to observe a planar image of the flow density with the Rayleigh signal allowed the easy identification and rejection of particles that had plagued the earlier point studies. The imaging version has become common practice. After a subsonic demonstration [2] of planar density measurement, the method was applied often for combustion and non-reacting flows [see citations in Refs. 1 and 3]. Less often an alternative version of RLS was used for simultaneous measurements [4, 5] of flow density, temperature and velocity derived from the spectral line shape of the Rayleigh scatter. Only the planar density version of RLS is discussed here.

To better approach flight conditions with large Reynolds numbers, transonic and supersonic wind tunnels are designed to run at thermodynamic conditions near the condensation curve of the gas medium. One potential problem with the RLS diagnostic occurs when significant cooling of the flow medium in the nozzle expansion results in the onset of clustering [6], i.e. the beginning stages of condensation from gas to liquid. Here the term clustering is loosely used to mean that a small fraction ($\leq \sim 0.1$ %) of the gas molecules has condensed into small clusters ($\sim$ tens to millions of atoms per cluster), with the vast majority of the flow remaining in the diatomic molecule form. The clusters are small enough that they are not individually resolvable with visible light, and the scattering is in the Rayleigh regime (laser wavelength $\lambda \gg$ cluster diameter D). Clusters are distinguished from particles that are bigger, are individually resolvable with visible light, and scatter light in the Mie regime ($\lambda \ll$ particle diameter D).

Although a tiny mole fraction of clusters may not change the bulk properties of the flow, they are uniformly distributed and can be considered a minor component of the fluid, similar to Argon in air. In the Rayleigh regime, a single scattering center has a differential scattering cross section $d\sigma/d\Omega$ that increases with size to the sixth power:

$$d\sigma/d\Omega \propto D^6. \qquad\qquad (1)$$

This strong increase in scattering with size means that a small fraction of clusters in the sample volume can increase the strength of the total light scattering beyond the pure molecular Rayleigh level. Since clusters are not typically resolvable in visible-light images, the extra scattered light from the clusters cannot be distinguished from the

molecular scattering and constitutes an error in quantitative measurements of the fluid density by RLS. This effect was apparent in early studies in supersonic flow [3, 7-9], where the elastic light-scattering from clusters provided a strong signal; thus the data could be used for only qualitative flow visualization (i.e. relative flow density maps). Absolute quantitative density measurements from a molecular signal of RLS were not possible in these early works because of the presence of the clusters.

At NASA Langley Research Center (LaRC), laser-based RLS has been used in several flow facilities, including hypersonic tunnels [10]. Although recently no clustering was observed for typical run conditions in one particular Mach-10 facility [11], this is a rare occurrence. References 8-10 indicate that most hypersonic facilities investigated at LaRC exhibit significant clustering in the free-stream flow for most run conditions. Clustering has also been observed in non-LaRC hypersonic facilities that utilize pure N_2 instead of air [12] as the flow medium.

At lower speeds, RLS has also been demonstrated [13, 14] at the LaRC 1/3-meter transonic cryogenic facility (TCT), where no clustering was found for all run conditions tested. TCT was built as a prototype for the National Transonic Facility (NTF), which is a large-scale cryogenic facility that is used to test at uniquely large Reynolds numbers – closer to flight-Reynolds number than other typical non-cryogenic wind tunnels. Due to the importance of NTF and the desire for additional flow diagnostics, it is a natural to ask if the flow at NTF is also clustered as in hypersonic tunnels, or not clustered as in the 1/3-meter facility. The answer impacts the diagnostic potential of RLS at NTF.

RLS can also help with characterization of the wind tunnel flow, in particular with the particle component. Particle flux is important because boundary layer transition from laminar to turbulent flow is influenced by entrained free-stream particles. Impinging particles on leading edges may pit or adhere to otherwise smooth surfaces [15-17], inducing early boundary layer transition. From low-speed liquid-water [18] to hypersonic air [19] and by-pass transition studies [20], the particle influence on transition is an important area of study [16, 21]. Characterization of particulates was recently reported [22] in another large-scale cryogenic facility, the European transonic wind tunnel (ETW).

Present Work

An exploratory experiment was performed to test the feasibility of RLS as an off-body flow density diagnostic for cryogenic N_2 (cryo-mode) and heated-air runs (air-mode) in NTF. Both side-scattering and back-scattering Rayleigh results are used to determine if the flow exhibits clustering or remains in the purely diatomic molecular phase. Lack of clustering implies that RLS remains viable as a quantitative flow diagnostic. The focus here is on whether or not RLS can be used for a quantitative flow density mapping.

The RLS apparatus automatically detects Mie scattering, without modification, and was used to directly visualize the naturally-occurring particles that are present in the

flow. Estimates of the free-stream particle flux are presented for both cryogenic and non-cryogenic flow conditions. These particle flux measurements may be useful for boundary-layer transition studies (e.g. [23]) and providing particle-content information as a part of a general effort to assess the NTF free-stream flow quality [24-30].

The light scattering work was conducted in a piggy-backed effort, where all optical measurements were acquired in the free-stream, about 30 cm in front of the model of a regularly-scheduled test. Propagation of the laser beam through the free-stream flow was unobtrusive to the flow and aeronautics test in progress. After preparation of the optical setup beforehand, there was no intrusion or interruption to the primary portion of the test; real-time test decisions were made by the primary user. The optical testing was essentially independent of the main test. This document describes only the optical RLS work and data and reports on a novel measurement in NTF that promotes diagnostic development and sheds light on the nature of the NTF free-stream flow.

II. Experimental Setup for Light Scattering

Wind tunnel

The present work was performed in NTF at LaRC. NTF is a closed circuit, fan-driven, cryogenic wind tunnel that generates transonic flow from Mach number $M = 0.1$ to $M = 1.2$. The tunnel uses air or pure N_2 as the working fluid. In air-mode, the air flow medium is modestly heated in the stagnation region, and in cryo-mode, liquid N_2 is regularly injected into the flow circuit. After purging of the air, this provides a pure N_2 flow fluid with total temperatures T_t down to as low as -250 deg F = 116 K. The present work was performed in both cryo-mode (T_t = -50 °F = 237 K) and air-mode ($T_t \approx$ +130 °F = 327 K). Total pressure P_t was varied between 20 and 55 psi. M varied mostly between 0.5 and 0.9, with some limited time at $M = 0.1$. Additional information on NTF can be found in References 24 and 31.

Model

The nature of the test, model, and results are proprietary. Here, descriptions of the experiment and model are intentionally vague or omitted to maintain confidentiality of the user. This report describes only optical results, mainly independent of the primary test. However, the model contained blowing ports for high pressure gas. This blowing slightly influenced the light scattering results, and optical results with blowing from two of these ports, hereafter called port 1 and port 2, are discussed.

Optical Arrangement

The optical arrangement and some of the equipment used in the present work was left over from a previous effort to develop a seeded-velocimetry diagnostic [32] at NTF using near-backward scattering. After the velocimetry work ended, part of the equipment was left installed in the wind tunnel. Due to the limited resources available for the current RLS effort, the leftover equipment from the velocimetry project was slightly

modified and adapted for the present work. Thus some geometry and some of the experimental parameters of the present RLS work were partially determined by the earlier velocimetry work and may not be optimum for RLS. In general, the limited optical access to the test section is a challenging obstacle for optical diagnostics in this facility.

The optical setup is summarized in the schematic of Figure 1. NTF has a double-walled test section, with the outer wall (16-ft diameter) acting as the pressure vessel and the inner slotted-wall defining the test section. Only the inner wall is depicted in Figure 1. The test section is square, about 8.2 ft (2.5 m) by 8.2 ft. A 532-nm wavelength continuous-wave laser is located in a laboratory near the test section. The laser beam is injected into an optical fiber (orange) that is used to bring the beam through the outer-wall pressure shell, through the high-pressure plenum, and to the test section inner wall. The beam is directed through a 4-ft (1.2 m) focal-length lens mounted on the ceiling of the inner wall. Located about 30 cm in front of the leading edge of the model, the beam propagates vertically downward through the test section (vertical dashed blue line) and focuses roughly on the centerline of the test section where the minimum beam size is about 500 μm in diameter. The beam continues downward and hits the floor of the test section where it scatters significant stray light all throughout the test section. With the laser producing 8 W, about 3.5 W is delivered into the test section.

A second lens (50-mm diameter), immediately next to the lens that focusses the incoming laser beam, is used to collect light scatter in the near-backward direction as shown in the Figure 1 (slanted dashed blue line to the left of the laser beam). The scattering angle is about 178 degrees with respect to the laser beam propagation. This collected back-scattered light is directed through a second fiber (red) to a detector, which is a photomultiplier tube (PMT) that is located in the same room as where the laser is located. The bare PMT with a 50-ohm load resistor would normally have a time response of about 10 ns, but in this case the response was artificially slowed with a 20 kHz low-pass filter with an RC time constant of about 50 μs. The signal voltage is digitized every 5 μs (200 kHz) and recorded on a storage oscilloscope to provide 20-ms-long temporal histories (4096 points) of backward light scattering. The PMT, two optical fibers, and side-by-side lens pair mounted on inside wall of the test section are the equipment leftover from the velocimetry project.

A second detector, a cooled charge coupled device (CCD) camera, is placed in an environmentally controlled box in the plenum, in front of window on the side of the inner wall. The height of the camera off of the floor is 4 ft (1.2 m), allowing observation of the laser beam near the tunnel centerline region. A 50-mm diameter camera lens is used to image approximately 50 cm of vertical extent of the laser beam onto the 20 mm CCD chip with a magnification of about 24 (shown by two approximately horizontal blue dashed lines in Figure 1). This camera detects side-scatter Rayleigh at a scattering angle of 90 deg with respect to the propagation direction of the input laser beam. Whenever optical data is desired, near simultaneous data acquisition for both camera images and PMT time traces is manually triggered from the control room. Most of the data presented here are from side-scatter images from the CCD camera, but some back-scatter temporal waveforms from the PMT are also discussed.

III. Results and Discussion

Section III contains two results: the first in part A is a measurement of the strength of the Rayleigh scattering to distinguish molecules and clusters, and the second in part B is a Mie-scattering measurement from the naturally-occurring particle flux.

III A. Is Clustering Observable in the Free-Stream Flow?

Side-Scatter

Figure 2 shows two examples of typical images of the laser beam in the wind tunnel test section. Two circular features (one bright and one dim) in each image are windows in the sidewall of the test section, while the leading edge of the model appears on the right side of the images. The bright thin vertical line is the laser beam. The right-side image is cryo-mode with the flow on (T_t = -50 °F, P_t = 54 psi = 3.7 atm, and M = 0.81) and illustrates five particles (arrows) passing through the beam in the 20 ms exposure. Except for the five particles that generate Mie scatter, the rest of the beam is particle free and is visible by Rayleigh scattering. The left-side image shows the beam with flow off, a few minutes after the fan has been shut off. When the fan is turned off, it typically remains turning at a very slow speed (3 rpm) to maintain some minimal circulation of the fluid inside the tunnel, but the flow can be assumed to be essentially zero. In contrast to the right-side image, the left-side image shows a myriad of particles in the beam (too many to count or even distinguish) and these particles are always observed to diffuse into the beam within a minute after the fan is shut off. The concentration of these particles is similar to the large concentration of dust particles in typical room air. Mie scattering from particles in the left-side image dominates and precludes a confident measure of the Rayleigh scattering from diatomic molecules, however the right-side image with flow on is usable. When the flow is established, the particle density quickly decreases to the typical example shown in the right-side image.

The expected Rayleigh light scattering signal N_{sig} from a known diatomic molecular density is well known. The number of photoelectrons generated by the detector photocathode, during a single exposure, N_{sig}, is given by

$$N_{sig} = \eta_{QE} \, T_{sig} \, T_{beam} \, E_{beam} \, N \, \Omega \, (d\sigma/d\Omega)_{90} \, L_{vert}, \qquad (2)$$

where η_{QE} is the quantum efficiency of the photo cathode on the camera, T_{sig} is the fractional transmission of the scattered signal light from the beam to the camera cathode, T_{beam} is the fractional transmission of the laser beam from the internal power meter of the laser to the sample volume in the test section, E_{beam} is the energy of the beam transmitted through the test section during the exposure, N is the number density of the scattering molecules in the sample volume, Ω is the collection solid angle defined by the focusing lens that images the beam onto the camera, and L_{vert} is the extent (along the beam propagation direction) of the beam that is imaged onto the detector, accounting for the optical magnification. With the camera observing at a right angle to the beam, the diatomic Nitrogen differential cross section at 90 deg $(d\sigma/d\Omega)_{90}$ is used. All of the

parameters on the left side of Equation 2 can be estimated and the expected Rayleigh signal can be calculated with an uncertainty estimated to be about a factor of two. The free-stream density N is determined from the standard traditional pressure and temperature wind tunnel instrumentation. This calculation is then compared to the measured RLS signals to look for the presence of clusters. Close agreement indicates no clusters, while a measurement larger than the calculation indicates the presence of clusters with increased scattering cross sections.

Images like that of the right-side of Figure 2 are used to measure the actual strength of the light scattering of the laser beam, since the few particles in the beam can be easily avoided. Figure 3a shows a schematic of the focusing of the beam onto the camera CCD active area. About 430 μm of beam vertical extent is imaged onto a single 18 μm pixel on the camera (this camera actually has 9 μm by 9 μm pixels, but 2 by 2 binning was used throughout this work, so in this analysis the pixel size is taken as 18 μm). After selecting a vertical location on the beam without particles, an 80 pixel horizontal window, centered on the beam is summed to determine the integrated light scatter (i.e. the integrated photoelectrons deposited on line of pixels spanning the beam) across the beam at that location. The beam is typically 20 pixels wide, so the 80-pixel window provides plenty of background for subtraction. This measurement is limited by various uncertainties and the total is estimated to be about a factor of 1.5. Last, the measurement is compared to the expected molecular signal from Equation 2 to decide if the light scatter is close to the Rayleigh level. Comparing measured to calculated molecular signals with the simple ratio Q = measurement / calculation, then Q has a total uncertainty of about a factor of three. With these large uncertainties, values of Q of ≈ 0.3 – 3 are consistent with pure molecular scattering, while Q > 3 indicates probable clusters and Q < 0.3 is very unlikely and indicates an error in the data or analysis.

In principle it would be better to partially evacuate the test section to series of known densities (w/o particles) and calibrate the RLS instrument in situ. This is typically done in other facilities [10] and can provide the absolute sensitivity of the Rayleigh instrument to about a few per cent, better than the factor of three quoted above using Equation 2 and the comparison method. However, NTF is an unusual situation. Although the test section cannot be partially evacuated, it can be pressurized. More importantly, as soon as the fan is turned off for a no-flow condition, a large number of particles immediately starts to diffuse through the laser beam and will contaminate a pure Rayleigh signal with Mie scatter. This occurs in both air and cryo-modes. Because of this problem, it is convenient to use the rough comparison method (although it is much less accurate) instead of a calibrated instrument approach, which appears difficult in NTF. The calibrated detector approach was used previously [13, 14] in TCT where particles were essentially absent and not a problem.

The result of a single measurement of the absolute level of the light scattering is given in Figure 3a. For this single 20-ms image, Q = 700 / 310 = 2.3 for run conditions T_t = -60 °F, P_t = 50 psi = 3.4 atm, and M = 0.11. This data point is the left-most point in Figure 3b, where five single-image results are plotted for two cryo-mode and two air-mode conditions. The two left-most points are for the same cryo-mode condition and

illustrates the typical reproducibility for single-image data. Finally Figure 3c shows 27 test points for seven different run conditions (four cryo-mode and three air-mode), where each data point is now the average of 10 different images taken over several seconds of constant run condition. The four different averaged points within each constant run condition (i.e. single color) also show good reproducibility. Six runs give ratio Q between approximately 0.5 and 2, well within the uncertainty (a factor of three) stated above. One air-mode run shows $Q \approx 4$ and may indicate either clustering or an unknown error in data acquisition or analysis. But the general conclusion is that clustering cannot clearly be detected with the present data – the fluid is essentially diatomic.

Back-Scatter

The above side-scatter results can be checked using backscatter results that were acquired nearly simultaneous with the side-scatter data. By nearly simultaneous it is meant that the backscatter and side-scatter data acquisition were always taken within several seconds of each other during constant run conditions, but not simultaneous to within 20 ms, which was the data acquisition window length for both detectors.

Examples of three backscatter data acquisitions at three different run conditions (two cryo-mode and one air-mode) are shown in Figure 4. Each trace shows the backscatter signal on the PMT detector of Figure 1 for 20 ms. The green trace shows one cryo-mode acquisition that shows two different particles transiting the beam as two short spikes (3-5 data points wide $\approx$ 20 us) in scattering intensity that spike upward on top of the average long-term scattering level. The transit time of a typical particle through the laser beam is estimated to be about

$$T_{transit} \approx \text{beam diameter} \div \text{flow velocity} \sim 500 \ \mu m \div 200 \ m/s = 2.5 \ \mu s. \qquad (3)$$

The observed transit times of $\sim$ 20 μs are closer to the slow time constant of 50 μs for the PMT than to the faster flow transit time estimate of 2.5 μs of Equation 3. The vertical scale in Figure 4, including zero that represents approximately no light scattering, is for only the green trace. Electronic and optical backgrounds are negligible on the scale of Figure 4. Thus the green arrow on the right-hand side of the figure illustrates the level of Rayleigh scattering for the green run. The other two traces had roughly the same continuous scattering level as the green trace, but have been arbitrarily shifted vertically (purple down and red up) to make all three traces clearly visible by minimizing overlap. The air-mode purple trace shows one particle, and the red trace shows no particles present for that particular 20-ms observation.

To further test if the RLS signal is proportional to the diatomic molecular density (i.e. the absence of clusters), the relative fractional signal change is plotted versus the relative fractional density change in Figure 5. A large fraction of the runs for this particular test were made at nearly the same static densities that would not allow a reasonable test of this nature. However a small fraction of the total test data was acquired as the flow density was changed significantly over a short period of time. This small portion of the data is shown in Figure 5 for both backscatter and side-scatter.

Five data points (each averaged over 20 ms) of backscatter are shown, along with eight nearly-simultaneous side-scatter points (each averaged over ten 20-ms images). The dashed line represents a linear one-to-one fractional increase of signal with fractional density, which is expected without any clustering. Both data sets (using independent detectors) show scattering signals that increase roughly linearly with density. An estimate of the statistical error is $\pm$ 10% which is based on a simple visual inspection of the differences between the dashed line and individual data. Neither data set appears to systematically deviate from the dashed line by more than several per-cent, and provides an estimate for the upper limit of clustering. One expects an increase greater than the linear dashed line if clustering was just beginning, and expects a nonlinear signal increase if clustering was occurring to a significant degree. The Figure 5 result implies that clustering is probably not contributing more than a few per-cent of the total signal and is consistent with the result of the side-scatter-only result of Figure 3c. Again, as in the previous section, the conclusion is that the fluid is mostly diatomic in nature.

Summarizing the cluster portion of this report, the result of Figure 3c shows that the measured Rayleigh signal is approximately equal to the calculated (i.e. expected) Rayleigh signal from Figure 3a. The uncertainty in the calculation is about a factor of two and the uncertainty in the measurement is about a factor of 1.5. Thus the measurements mostly agree with the calculation, well within the estimated combined uncertainty of a factor of three. The result of Figure 5 shows that the observed relative change in measured Rayleigh signal is linearly proportional to the flow density to within an uncertainty of $\pm$ 10%. Based on Figures 3 and 5, the conclusion is that there is little clustering – not more than that equivalent to 10% of observed scattering signal and probably even less. Additional measurements with increased precision are required to rule out clustering at levels of smaller than a few per cent of the total scattering signal. The absence of clusters in NTF is consistent with earlier results [13, 14] of no clustering in TCT, which also uses cryogenic flow at similar pressures and temperatures.

This conclusion of no observable clustering in NTF is the primary result contained in this study. A future experiment, with larger signal-to-noise ratio (SNR) and some limited wind tunnel runtime priority is required to rule out clustering to a level closer to zero than is possible with the modest SNR of the present piggy-backed effort. The next section contains the secondary result of this report: direct visualization of the particles in the free-stream.

III B. Observation of Naturally-Occurring Particles in the Free-Stream

Back-Scatter

Figure 6 shows more sequences of near-backward scattering into the PMT detector for cryo-mode. The green trace in Figure 6 is identical to the green trace of Figure 4, corresponds to the vertical number scale (including zero) as shown, and is included for comparison purposes. Black, red and blue traces show three additional examples of 20-ms snapshots and are arbitrarily offset vertically to minimize overlap of

the different traces. While the examples of Figure 4 showed only ~ one particle per 20-ms trace, the black and red traces of Figure 6 show about 20-30 particles per 20 ms. Assuming that the length of laser beam (with average width ~ 1 mm) contributing to these signals is about 50 mm, runs like those of Figure 4 correspond to ~ 1 particle / (sec mm^2), while the black and red traces of Figure 6 correspond to ~ 30 particles / (sec mm^2). In the next section, particle flux versus several flow and model parameters is displayed to convey a sense of how strongly they may affect the particle environment.

Side-Scatter

Figure 7 shows another example of direct imaging of the beam from the side direction, with three particles transiting the laser beam in this 20 ms exposure at cryo-mode of -50 °F. This right-hand side of this example is at M = 0.7 while the previous example of Figure 2 was at M = 0.8. Again, with the flow off (fan ~ 3 rpm), the particles visible in the beam immediately increase as shown in the left-hand image.

Figure 8 shows a third example of direct imaging of particles, this time at the air-mode condition of +120 °F. The right hand image shows no particles in this image (note the factor of two decreased field of view for the right-side image), although particles are often present in air-mode. The left-hand image of no flow again shows an increase (less than the two previous cryo-mode examples, but still significantly above nonzero) in particles as soon as the fan is turned off. This argues that the increase in clusters for fan-off status is not necessarily due completely to thermodynamic-related clustering, even in the previous cryo-mode conditions.

After manually counting (visually inspecting the images, spending several seconds per image) the particles in a few thousand images spread out over a variety of run conditions, a computerized method based on commercially available software packages was put together to automatically count the particles in the laser beam images. This routine worked well for cryo-mode, where the particles are typically larger and brighter than air-mode, but did not work for the smaller and dimer particles in air-mode. One benefit of the time-consuming manual counting is that a good feeling for the raw data is obtained. Relying 100% on automated counting may increase the possibility of missing important features of the data set.

For this particular test, generally one or two test points were recorded for each new run condition, which corresponded to a given M, T_t, P_t , AoA, and blowing condition. Blowing ports for gas injection from the LaRC bottle-field, were located at two locations (port 1 and port 2) on the model to fulfill certain test objectives. In this test a full run (i.e. 5-15 test points) is defined by varying the angle-of-attack (AoA) over the range of interest and taking one or two test points at each AoA, which normally took about 5-10 minutes. For the RLS experiment, for each test point, a few sets of ten 20-ms side-scatter images were recorded, where each set of ten images was obtained over an interval of several seconds. Particle flux estimates for each test point were made by averaging over the ten successive images for at least one full set of ten images. Since the observation region for the side-scatter images is ≈ 1 by 50 mm = 50 mm^2, only a very

small fraction of the total cross sectional area of the test section, (about 8 ft by 8 ft $\approx$ 4 x 10^6 mm^2) is interrogated. These absolute values of particle flux should be taken as an order-of-magnitude estimate due to the uncertainty in the sample volume size and the very small fraction of cross sectional area probed.

Typical examples of particle flux estimates made by manual counting are shown in Figure 9 for seven different air-mode runs (+130 °F) and seven different cryo-mode runs (-50 °F), where there is one run per symbol type (air-mode open boxes and cryo-mode filled triangles). Each point is an average over ten successive 20-ms images and the various runs correspond to a variety of total pressures. The horizontal axis, labeled as data point number, does not correspond to any physical run parameter and serves only to distinguish different data points in no particular order. The large variation in amplitude for a typical cryo-mode run is not noise, but corresponds to varying AoA that will be shown in detail in later figures. The purpose of Figure 9 is to show that a much greater particle flux is typically observed in cryo-mode than in air-mode.

The AoA dependence for the cryo-data is better seen in Figure 10, which shows four results of averaging some of the data from Figure 9 over a few runs and plotting versus AoA on the abscissa. The filled blue boxes show an average of four air-mode runs with no AoA variation. The filled red triangles show a short scan over AoA with an average of four cryo-mode runs, while the filled green diamonds show another average over just two cryo-mode runs – both with a clear AoA variation. But the open black triangles show a third average over two different cryo-runs with only a weak AoA variation. Again the difference between air-mode and cryo-mode particle characteristics is illustrated. Cryo-mode runs generally show more particles, often with a clear AoA dependence, while air-mode runs show less particles with approximately little or no AoA dependence.

Manual counting of particles contains systematic errors related to the individual characteristics of the human observer. Many of the rest of the results given here were obtained in a more subjective manner with a computer-based automated counting of the particles. Before proceeding on to show these results for a variety of flow conditions, a quick comparison of manual and automated counting is given in the next two figures. Figure 11 show a comparison of manual counting between two observers denoted by GCH and MPV, where reasonable agreement (run 260) was typically found between the two observers. When there was disagreement (e.g. run 280), MPV counts were typically a little larger than those of GCH. Comparison of techniques of the two observers revealed that MPV spent more time per image, consistent with MPV finding more particles. On one occasion when GCH recounted run 260, spending more time per image, the counts of GCH increased to approximately those of MPV.

In Figure 12, which shows a comparison of manual counting by GCH versus the computer program, the automated method found about three times the number of particles as GCH did. This figure shows AoA scans for four blowing conditions, denoted by nozzle pressure ratio (NPR) at port 1 on the model. Note difference of vertical scales on the two plots. Automated counts typically find two to three times the number of

particles as from manual counting and are considered to more correct, in terms of the absolute number of particles found. Although the automated routine occasionally finds a particle when there is none, this type of error was found to be small (by spending much more time than a several seconds per image and carefully manually inspecting a few images) compared to missing particles by manual counting.

The uncertainty in these particle flux measurements is large. Among other lesser contributions to the total uncertainty, the primary systematic error is due to the fact that only ~ 1/1000 of the test-section cross-sectional area is being interrogated. From a statistical point of view, a factor of 10 variation (or more) is often observed for image-to-image fluctuations in the particle flux. The uncertainty for particle flux data reported here is very roughly estimated to be about a factor of 10.

Variation of Particle Flux with AoA and NPR

Figure 13 shows the results of automated particle counting for about 50 scans over AoA. All scans are cryo-mode at -50 °F, but for a variety of P_t ranging from about 20 to 55 psi (i.e. 1.4 to 3.7 atm). Each point is an average over 10 successive images. Many scans show little or no AoA dependence. Many other scans show a clear "u" shaped dependence on AoA with the minimum particle flux occurring near +3 deg AoA. The scans with the obvious "u" shaped dependence on AoA are one of the only a few times a clear particle flux dependence was found in this work. Increased gas densities often lead to increased condensation processes and the AoA dependence of Figure 13 might be related to the flow density. To decide if this AoA dependence is related to the flow density, each curve of Figure 13 is fit to a simple quadratic function

$$y = Ax^2 + Bx + C, \qquad\qquad (4)$$

where A, B, and C are constants, y is the particle flux, and x is the independent variable = AoA. The size of A indicates the degree to which there is a strong nonlinear AoA dependence. Using A values determined from the fits of Figure 13, A is plotted in Figure 14 as a function of R, the Reynolds number per foot, and hence as a function of mass flow rate or total gas density since R ∝ dm/dt. Although the correlation of Figure 14 is suggestive, it is not strong and confidence inspiring. Thus it is not clear if the degree of AoA dependence observed in Figure 13 is a really dependent or not on R and its related parameters such as mass flow. But clearly in Figure 13, some runs show a strong AoA dependence for one reason or another.

All data points in Figure 14 have been averaged over an AoA range of -5 to +15 deg. To show that averaging is not the reason for producing the poor correlation, Figure 15b shows results averaged over only +5 to +10 deg AoA, while Figure 15a shows data at only 3 deg (approximately the AoA of minimum particle flux) without any averaging. Particle flux data of Figure 15 are plotted versus free-stream flow mass flux, but the plot is equivalent to Figure 14 since Reynolds number is proportional to mass flux. Results of the two figures are similar. Thus the inconclusive (i.e., suggestive but not convincing) correlation of Figure 14 is independent of the degree of averaging over AoA.

The model AoA dependence of most data in Figures 10, 12 and 13 is the first of two occasions when a moderate dependence for particle flux was found. The second instance of a correlation between particle flux and a flow parameter is with the blowing rate from port 1 (and no blowing from port 2). This is shown in Figure 16, where the same exact data set is plotted versus AoA in the plot of part (a) and verses nozzle pressure ratio (NPR) in part (b). Part (a) shows the aforementioned AoA dependence for six different NPR, while part (b) shows a clear NPR dependence for the seven AoA conditions. NPR = 0 corresponds to no blowing from the port. Although the NPR dependence is not strong, it may be real due to additional cooling in the model wake.

Summarizing, the only two cases of moderate (i.e. probably real, but not impressive) correlation between free-stream particle flux and another flow parameter is first with AoA as shown in Figures 12, 13, and 16 and second with blowing NPR as shown in Figure 16. One might have anticipated that a correlation between flow density, pressure and/or temperature would have been found because lower temperatures and higher pressures generally enhance condensation. But these potential correlations are even weaker than the two modest correlations with AoA and NPR. To illustrate the sometimes suggestive, but not convincing, correlations, the next 11 figures show the particle flux dependence versus a variety of flow conditions (including P_t and T_t).

Variation of Particle Flux with P_t and T_t in Cryo-Mode

Figure 17 is the first of these and shows the free-stream particle flux versus the injection rate of liquid N_2 into the tunnel. As the tunnel runs under constant cryogenic flow conditions, it is constantly losing heat to the outside environment, and additional liquid N_2 is periodically injected into the fluid stream to maintain the desired set point. Each point in the figure is an average over a scan over one complete run (i.e. one scan over AoA, or an average over about 200 single images). Figure 17 shows the suggestive, but not convincing, trend of observed particles with increasing injection rate. Note the run condition for these many points varies with the injection rate.

Figure 18 shows how the free-stream particle flux varies with Mach number for cryogenic conditions. Each point is an average over 10 successive images, and the wide variation over each run (i.e. each type of symbol) in the Mach 0.7-0.8 region is due to the AoA changing from point to point, while total temperature $T_t = -50$ °F. The variation over of the two runs at Mach 0.1 is because the temperature is decreasing from point to point (i.e. the tunnel is being cooled down and AoA is constant at near zero). Again, the very weak correlation is suggestive but not convincing.

Figure 19 shows cryogenic free-stream particle flux as a function of total density (part a) and total temperature (part b). Each part show two runs, where for the first run (red squares) total temperature is varied and for the second run (blue diamonds) nothing is varied except for a few points with reduced total pressure, which is obvious from where they are plotted on the abscissa. Thus for the blue diamonds, nothing much

14

changes and the particle flux varies from zero to about 0.4 particles / (mm^2 sec). There is no obvious dependence of particle flux in either plot.

Figure 20 shows two plots of the same data set, the cryogenic free-stream particle flux dependence on either static P_s (green diamonds) or total pressure P_t (red bars). These data were taken so that variations in Mach number and total pressure approximately canceled and static pressure was constant, except for a few points. Each point in this figure is an average over AoA of -5 to +10 deg, and ten successive images at each AoA were used. Thus each point represents the average over about 100 images. Again the large variation of particle flux over constant P_t or P_s suggests little relationship between pressure and particle flux.

Figure 21 shows cryogenic free-stream particle flux versus static density of the flow in three different plots for the same data set. First in the top plot (a), data from eight runs with each individual point representing a single AoA. In the lower left plot (b) the number of runs used has been increased to 50 and the data over AoA from -5 to +10 deg is averaged into one point. Finally, in the lower right plot (c), data only at 3 deg AoA is plotted. The two lower plots show less absolute variation of particle flux for constant abscissa value, but even in these two lower plots the variation is still too much to claim a fixed particle flux with fixed abscissa. Thus again, there appears to be no clear dependence of particle flux on the static density of the flow.

Summarizing, Figures 17-21 have shown little correlation of particle flux with the thermodynamic condition (i.e. pressure, temperature, or density) in cryo-mode. In contrast, the next three figures show a better-quality case (but still not great) for a correlation between particle flux and P_t and T_t. First Figure 22 shows three sets of three runs over AoA, with varying Mach number and total pressure. In the first set of three scans of Figure 22a, the run with maximum Mach number M (i.e. minimum T_s) and maximum total pressure P_t shows the most particles at all AoA, while the run with minimum M and minimum P_t shows the least particles at all AoA. The same observation holds true for the second set of three scans in Figure 22b. In Figure 22c, the same observation almost hold true, with the exception that the run with maximum M and P_t shows less particles that the run with the second highest M and P_t.

In Figure 23a (top plot), eleven successive runs (i.e. scans over AoA) are shown with particle flux plotted versus AoA for runs 158-168. For the tenth run (run 167 shown with a red diamond on top of the green diamond) the P_t was increased from 22 to 35 psi and it is this run that clearly shows a larger particle flux than all of the other runs (green diamonds without red boxes). For run 168, immediately after run 167 with increased P_t, the P_t was reduced back to 22 psi. This same data is shown in a different manner in the lower plot (Figure 22b), where the particle flux, P_t, and liquid nitrogen injection rate are all plotted on an arbitrary scale on the vertical axis and versus the run number shown on the horizontal scale. In this plot, the data for each run has been averaged over AoA to produce a single point for each run. These averaged particle flux values are then plotted versus run number. Finally, P_t and injection rate are also plotted along the vertical axis along with particle flux. Thus the scale of the vertical axis is relative for all three plotted

quantities. Note that for the single run 167, where P_t is increased (and the liquid N_2 injection rate is also increased), the particle flux also increases, before returning to the previous lower value when P_t is reduced for the next run. P_t clearly affects the observed particle flux here. Note that Mach number is slightly changing throughout runs 158-168, from Mach 0.7 to 0.82, but is constant for three runs 166-168 at Mach 0.76.

Figure 24 shows a consecutive set of 35 runs over 2.5 hours. P_t and T_t were held constant at 50 psi and -62 °F from run 12 until run 20. For runs 21-24, the flow was temporarily heated to -47 °F (at constant Pt of 50 psi). Then beginning with run 25, the flow was returned to T_t = -62 °F. The observation is that the short-term heating clearly reduced the particle flux to near zero. In summary, Figures 22 -24 more strongly suggest a relationship between particle flux and flow pressure P_t and Temperature T_t in cryo-mode than was seen in Figures 17-21.

Possible Weak Correlation of Particle Flux to T_t in Air-Mode

Returning to air-mode, Figure 25a shows particle flux data plotted versus static density, while Figure 25b shows particle flux of other runs plotted versus total density. All runs in air-mode were made at either T_t = 120 °F or 130 °F for this test, and the data of Figure 25 were all acquired at a constant pressure of about P_t = 34-37 psi. Each plot in the figure shows data from both T_t values, where the two values are distinguished by notes and arrows in the plots. Each point in Figure 25 is an average over 10 successive images at a single AoA. The vertical variation of particle flux for each run shown is due mostly to noise in the measurement rather than the miniscule variation (possibly as small as zero) due to changing AoA. Note that in both parts (a) and (b) of the figure, the runs at 130 °F generally show slightly more particles than the runs at 120 °F, hinting that slightly higher air-mode T_t generates slightly more particles.

Do Long Wind Tunnel Runtimes Clean the Flow Circuit of Particles?

One question that arises after seeing the observed particles in this facility, is does the particle flux decrease after long periods of running, or in other words, does the tunnel clean itself after long runtimes or after a normal day of running? This question is addressed for both cryo and air-mode in the final three figures of this report.

In Figure 26, air-mode particle flux rate is plotted versus time of day. Each point is a single tunnel data point at fixed AoA, averaged over to images. Over this one-hour period, with a couple of wind-off breaks between the runs, there appears to be no sign of decreased particles with increased runtime. In Figure 27, cryo-mode particle flux is shown versus time of day over three successive runs, with no wind-off between the runs. Each run (a different color) shows the "u" shape because AoA is varied from -5 to + 10 deg over each run. Over this 25-minute period there is no obvious reduction in particle flux due to some kind of self-cleaning by the tunnel. Finally, in Figure 28, cryo-mode particle flux versus time of day is again shown for a longer period. Again no obvious sign of self-cleaning is seen. Note that throughout this particular test it was common to sit in a wind-off condition many times during the day, and hence periods with ~ 10 hours

of continuous running are not available. The main conclusion is that the longest runtimes observed here (~ 1 hour) show no clear sign of reducing the particle flux.

IV. Discussion of Particle Flux Observations

In this section, results of the particle flux data are summarized and some tentative conclusions are presented. However confidence in the conclusions is tempered because of the limited quality of the observed variations of particle flux with some flow parameters. In general, there is a modest correlation of particle flux with AoA, blowing NPR, P_t and T_t, while a correlation with R (and dm/dt) seems more doubtful.

The following scenario is proposed to roughly describe most of the particle flux observations during the present work.
a) Air-mode (+130 °F) has relatively less numerous (i.e. smaller number density) particles than cryo-mode (Figures 9 and10). These air-mode particles probably originate from dust from the insulating foam that resides inside the tunnel circuit (or possibly trace amounts of oil in the flow).
b) Cryo-mode (-50 °F) has relatively more numerous particles than air-mode (Figures 9 and 10). Nitrogen condensation around the pre-existing small foam dust particles (which act as condensation nuclei) in cryogenic conditions might increase the observable particles by increasing the size of all particles.
c) Cryo-mode has relatively larger particles compared to air-mode, consistent with ideas in (a) and (b). This conclusion is based on a subjective observation, during manual particle counting: cryo-particles are often significantly brighter than air particles.
d) Why does the observable particle density increase dramatically as soon as the flow is turned off (Figures 2, 7, and 8)? When a flow is established in the test-section, the particle density is rapidly reduced to the levels that we typically measure. The plenum "stores" other particles that are well-mixed in the near-stationary plenum gas. This gas (including the plenum particles) quickly flows and/or diffuses into the test section thru the slotted walls, after the fan is turned off, to give the observed rapid particle density increase.
e) Is the observed particle flux correlated to any test condition? The best particle flux correlation with a test parameter is for AoA of the model in cryo-mode, although the correlation is not consistent. Some runs (one run is one scan over AoA) show a strong correlation and some runs show no correlation with AoA. When the correlation is present, particle flux is larger for larger AoA (positive or negative) and minimum at about +5 deg. Possibly the expansion behind the model at significantly nonzero AOA further cools the wake flow and increases the condensation around the already existing particles – giving the AoA dependences shown in Figures 10-13. An alternative to this scenario is that there may simply be a uniform distribution of particles, and thus particle flux increases with increasing mass flux (see Figures 14 and 15).
f) The particle flux dependence on AoA mostly disappears for air-mode runs (Figures 10 and 11). There may be a small residual AoA effect in air-mode.
g) The second best correlation for particle flux is with blowing NPR in cryo-mode (Figure 16) – in this case the correlation is consistent but not as strong as for AoA.

h) Correlations with other test conditions are not as clear as the above two correlations in (e) and (g). Figures 18-21 tend to show no correlation with T_t, P_t, and M.

i) But, Figures 22-24 show a probable, but modest, particle flux dependence on both P_t and T_t and possibly M. The particle flux seems to increase with colder temperatures or larger-pressures, as expected if it is related to condensation.

j) Figure 25 shows slightly more particles at T_t = +130 °F compared to T_t = +120 °F, suggesting possibly that more heat from the larger T_t may help erode the foam insulation in air-mode.

k) Figures 26-28 show that typical longer runtimes (limited to ~ 1 hour by the often periods of wind off during this particular test) do not give any observable particle flux reduction by some kind of naturally-occurring self-cleaning by the wind tunnel.

The outline (a-k) above is admittedly speculative and should be taken only as a possibility. Further work is needed for confirmation. However, one clear fact is that there is a significantly observable particles flux in the NTF free-stream flow field. The magnitude of this flux moderately depends on some experimental parameters. Looking forward, what does this particle flux mean for testing in NTF? A caution for future boundary-layer testing, a proposal for a boundary-layer transition test, and a possible new NTF diagnostic are noted below.

A previous boundary layer transition study in NTF [23] has observed time dependent turbulent wedges on the leading edges of the model. Non-monotonic changes in transition, with time, were observed. Permanent pitting of the leading edge would explain a monotonic buildup of advanced transition. In contrast, icing or oil accumulation may explain non-monotonic changes. Another possible explanation for non-monotonic transition changes may be that free-stream particles occasionally adhere to the leading edge region, causing a local transition and creating a turbulent wedge. Then at some random time later, the particle is blown off the model by the flow and the turbulent wedge disappears. This idea and the observation of (i) above are consistent with the fact that Reference 23 reports increasing time dependent wedges, with higher Reynolds numbers. If this process occurs, then the particle flux dependence on AoA also becomes important for transition testing as a function of AoA. Typical experimental studies of boundary-layer transition could be affected by this artificial wind tunnel effect in addition to the flow physics.

A simple test, to confirm this effect, is to illuminate the leading edge of a model with a continuous laser (1-10 W at 532 nm for example) and observe the ongoing sticking and unsticking of individual particles on the model with a camera. This was demonstrated previously in the Unitary Plan Wind Tunnel (UPWT) at LaRC [3]. The particle observation measurement could be done simultaneously with a traditional boundary layer transition technique (e.g. see [23]) to look for a correlation between particle sticking and transition detection with the traditional instruments.

If the sticking-particle scenario is relevant and is one cause of time dependent local boundary layer transition in cryo-mode, then a potential future diagnostic for the NTF facility is suggested. Use the setup of the experiment described in the previous

paragraph as a real-time diagnostic to detect particles sticking to the forward portions of the model. This would alert the tunnel personnel and researchers to a potential bypass transition situation like those observed in NTF [23].

V. Summary

A preliminary laser-based Rayleigh light scattering (RLS) experiment was performed in the National Transonic Facility (NTF) at NASA Langley Research Center. The goal was to determine if the free-stream flow medium undergoes clustering (i.e. the early stage of the condensation process from gas to liquid) or remains in a pure diatomic molecular phase. The main method used was optical imaging (at 90-deg viewing angle) of a laser beam that transited the tunnel test section. The 90-deg viewing data was augmented by simultaneously acquiring additional Rayleigh scattering signals in the near backward direction at $\approx$ 178 deg, relative to the incident laser beam transmission.

The present data indicate that clustering does not occur to a significant degree at a variety of total pressures for one N_2 cryogenic-mode total temperature (T_t = -50 °F = 227 K) and one air-mode condition (T_t = +130 °F = 327 K). This conclusion is based on a comparison of the measured and calculated (i.e. expected) RLS signals, by observing that the measured signals agree with expected Rayleigh signals. The presence of clusters would give light scattering signals larger than expected. Considering the uncertainties in the measurements and the calculations, less than ~ 10 % of the total scattering signal is due to clusters. This limit is an upper limit for the clustering signal and it is likely that there is no clustering at all, but that stronger conclusion would require an additional experiment with smaller uncertainties. Based on the results herein, RLS is viable as a quantitative diagnostic for flow density in NTF to within this stated uncertainty.

Additionally the RLS apparatus was used to visualize Mie scattering from naturally occurring particles entrained in the flow for both cryogenic and air-mode conditions. These particles are individually detected as near point-like objects in visual inspection of images of the laser beam. Estimates of the free-stream particle flux in NTF are presented for a variety of tunnel conditions. The particle flux is often dependent on the model AoA and weakly dependent on the NPR from one or two blowing ports that this particular model contains. Finally the particle flux is also sometimes dependent on the T_t and P_t of the run condition.

VI. Acknowledgement

VII. References

1.   Eckbreth A. C., Laser Diagnostics for Combustion Temperature and Species, 2nd ed., Gordon and Breach Publishers, Chapter 5 (Amsterdam, 1996).

2.   Escoda M. C. and Long M. B., "Rayleigh Scattering Measurements of the Gas Concentration Field in Turbulent Jets," AIAA J. **21**, 81-84 (1983).

3.   Herring G. C. and M. E. Hillard, Jr., "Flow Visualization by Elastic Light Scattering in the Boundary Layer of a Supersonic Flow," NASA Report TM-2000-210121 (August 2000).

4.   Pitz R. W., Cattolica R., Robbin F., and Talbot L., "Temperature and Density in a Hydrogen-Air Flame from Rayleigh Scattering," Combust. & Flame **27**, 313-320 (1976).

5.   Bivolaru D., Ötügen M. V., Tzes A., and Papadopoulos G., "Image Processing for Interferometric Mie and Rayleigh Scattering Velocity Measurements, " AIAA J. **37**, 688-694 (1999).

6.   Wegener P. P., "Cryogenic Transonic Wind Tunnels and the Condensation of Nitrogen," Exp. Fluids **11**, 333-338 (1991).

7.   Smith M., Smits A., and Miles R., "Compressible Boundary-Layer Density Cross Sections by UV Rayleigh Scattering," Opt. Lett. **14**, 916-918 (1989).

8.   Shirinzadeh B., M. E. Hillard, and R. J. Exton, "Condensation Effects on Rayleigh Scattering Measurements in a Supersonic Wind Tunnel," AIAA J. **29**, 242–246 (1991).

9.   Shirinzadeh B., Hillard M. E., Balla R. J., Waitz I. A., Anders J. B., and Exton R. J., "Planar Rayleigh Scattering Results in Helium-Air Mixing Experiments in a Mach-6 Wind Tunnel," Appl. Opt. **31**, 6529-6534 (1992).

10.   Shirinzadeh B., Balla R. J., and Hillard M. E., "Rayleigh Scattering in Supersonic Facilities," AIAA Paper 1996-2187 (AIAA, Advanced Measurement and Ground Testing Technology Conference, 19th, New Orleans, LA, (June 17-20, 1996).

11.   Balla R. J. and Everhart J. L., "Rayleigh Scattering Density Measurements, Cluster Theory, and Nucleation Calculations at Mach 10," AIAA J. 50, (2012).

12.   Griffith W. C., Yanta W. J. and Ragsdale W. C., "Supercooling in Hypersonic Nitrogen Wind Tunnels," J. Fluid Mech. **269**, 283-299 (1994).

13.   Shirinzadeh B., Herring G. C., and Barros T., "Demonstration of Imaging Flow Diagnostics Using Rayleigh Scattering in Langley 0.3-Meter Transonic Cryogenic Tunnel," NASA Report TM-1999-208970 (February 1999).

14. Herring G. C. and Shirinzadeh B., "Flow Visualization of Density in a Cryogenic Wind Tunnel Using Planar Rayleigh and Raman Scattering," NASA Report TM-2002-211630 (June 2002).

15. Stetson K. F., "Nosetip Bluntness Effects on Cone Frustum Boundary Layer Transition in Hypersonic Flow," AIAA paper 1983-1763, AIAA 16th Fluid and Plasma Dynamics Conference, Danvers, MA, (July 12-14, 1983).

16. Ladd D. M. and Hendricks E. W., "The Effect of Background Particulates on the Delayed Transition of a Heated 9:1 Ellipsoid," Experiments in Fluids **3**, 113-119 (1985).

17. Morkovin M.V., "Panoramic View of Changes in Vorticity Distribution in Transition Instabilities and Turbulence," Boundary Layer Stability and Transition to Turbulence, FED-114, 1-12. Eds. D.C. Reda, H.L. Reed, R. Kobayashi, ASME (1991).

18. Reshotko E., "Control of Transition – Heating and Cooling," NATO/OTAN RTO-EN-AVT-151 (1985).

19. Dunlap R. D., "Effects of Cooling on Transition in the Boundary Layer on a Hemisphere in Simulated Hypersonic Flow," PhD dissertation, University of Michigan (February 1961).

20. Jonáš P., O. Hladík, O. Mazur, and V. Uruba, "By-Pass Transition of Flat Plate Boundary Layers on the Surfaces Near the Limit of Admissible Roughness," 13th European Turbulence Conference (ETC13), Journal of Physics: Conference Series **318** (2011).

21. Schmidt C., T. M. Young, and E. P. Benard, "The Effect of a Particle travelling through a Laminar Boundary Layer on Transition," Seventh IUTAM Symposium on Laminar-Turbulent Transition, IUTAM Bookseries Vol. **18**, 2010, pp 561-564.

22. Christian Kühn, "Particle Counter - Cleanliness Assessment at ETW," unpublished, 118th STAI, Brussels, Belgium (14-16 Oct 2012).

23. Crouch J. D., M. I. Sutanto, David P. Witkowski, A. Neal Watkins, Melissa B. Rivers, Richard L. Campbell, "Assessment of the National Transonic Facility for Laminar Flow Testing" 48th AIAA Aerospace Sciences Meeting Including the New Horizons Forum and Aerospace Exposition, 4-7 January 2010, Orlando, Florida, AIAA paper 2010-1322.

24. Igoe, W. B. "Analysis of Fluctuating Static Pressure Measurements in the National Transonic Facility," NASA TP-3475 (March 1996).

25. Bobbitt, Jr. C. and Everhart, J., "Status of the National Transonic Facility Characterization (Invited)," 39th AIAA Aerospace Sciences Meeting & Exhibit, 8-11 January 2001 Reno, Nevada, AIAA paper 2001-0755.

26.   Complere Inc., "Measurement and Assessment of Flow Quality in Wind Tunnels," SBIR Phase II Final Report, Contract Number NN08AA12C, November 2009.

27.   Wlezien, R., White, R., Eppink, J., Liu, S., and Krause, J., "NTF Flow Quality Characterization for Laminar Flow Testing," Final Report for Task Order No. NNL08AM27T (072D3) September 2009.

28.   King R. A., M. Y. Andino, L. Melton, J. Eppink, and M. A. Kegerise and A. Tsoi, "Flow Disturbance Characterization Measurements in the National Transonic Facility (Invited)," 50th AIAA Aerospace Sciences Meeting including the New Horizons Forum and Aerospace Exposition, 9-12 January 2012, Nashville, Tennessee, AIAA paper 2012-0104.

29.   King R. A., M. Y. Andino, L. Melton, J. Eppink, and M. A. Kegerise, "Flow Disturbance Measurements in the National Transonic Facility," AIAA Journal **52**, 116-130 (2014).

30.   Owen F. K. and A.K. Owen, "Spectral Characteristics of Free-Stream Turbulence in the National Transonic Facility," 52nd Aerospace Sciences Meeting, 13-17 January 2014, National Harbor, Maryland, AIAA paper 2014-0617.

31.   Bruce, Walter E., Jr. 1985: The U.S. National Transonic Facility-Special Course on Cryogenic Technology for Wind Tunnel Testing, AGARD-R-722, pg. 15-1.

32.   Meyers J. F., A. A. Cavone, M. T. Fletcher, and J. W. Lee, unpublished (2008).
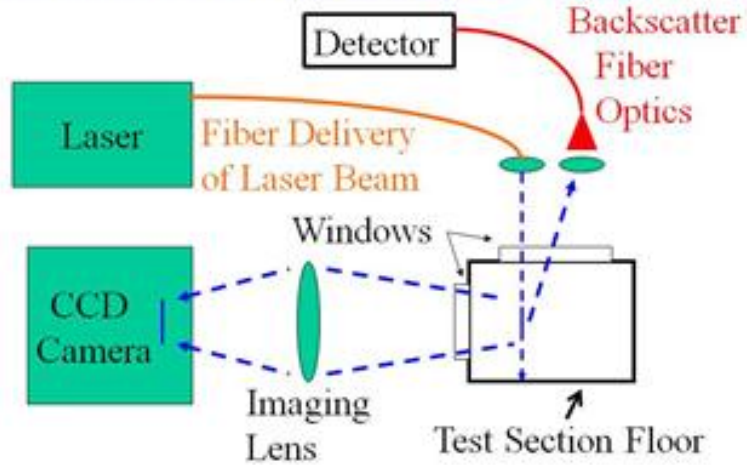
Figure 1. Schematic of setup for RLS in NTF in both the side (90 deg) and near backward (≈ 178 deg) directions with an approximately 10-W cw laser at 532 nm. Flow is out of the page.

Cryo-Mode Side-Scatter Results

Temperature = - 60 °F	T_t = - 50 °F
Flow Off	Mach 0.8
Medium Particle Density	5 Particles / 20 msec
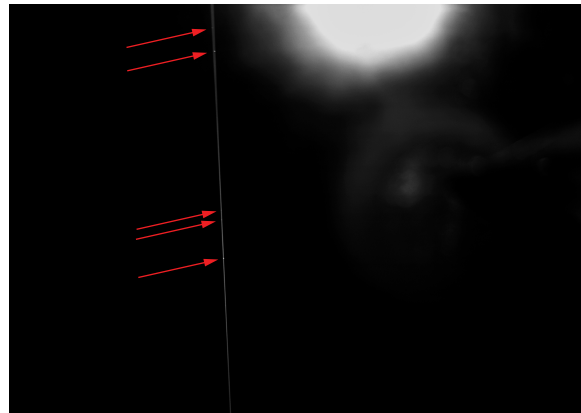
1474-0003   1790-0000

Laser beam width ≈ 1 mm
Exposure time ≈ 20 msec

Figure 2. Two examples of 20-ms images of the laser beam showing many particles in the flow-off image at left and 5 particles (red arrows) in the flow-on image at right.
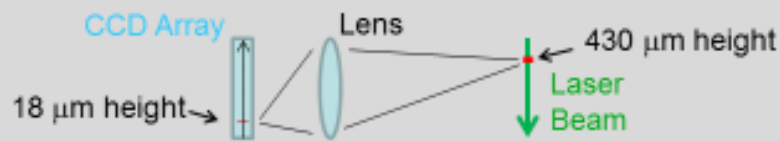
Figure 3a. Schematic of imaging the RLS side-scatter from the beam onto the camera, and one example of the result of comparing measured and calculated (i.e. expected) signals.
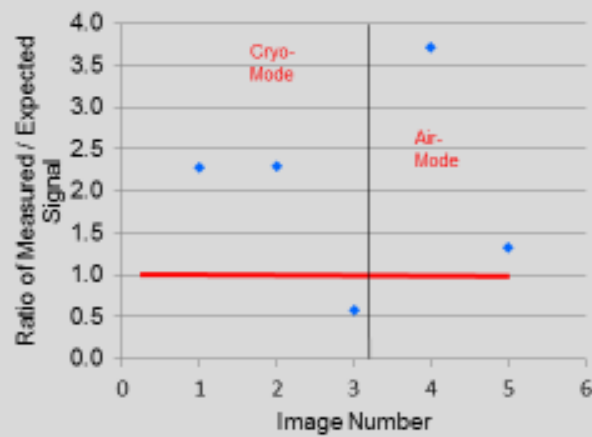
Figure 3b. Five examples of ratio Q (= [measured / calculated] RLS signal) for five single
20-ms images. A ratio near unity (indicated by red line) indicates no
clustering in the flow.
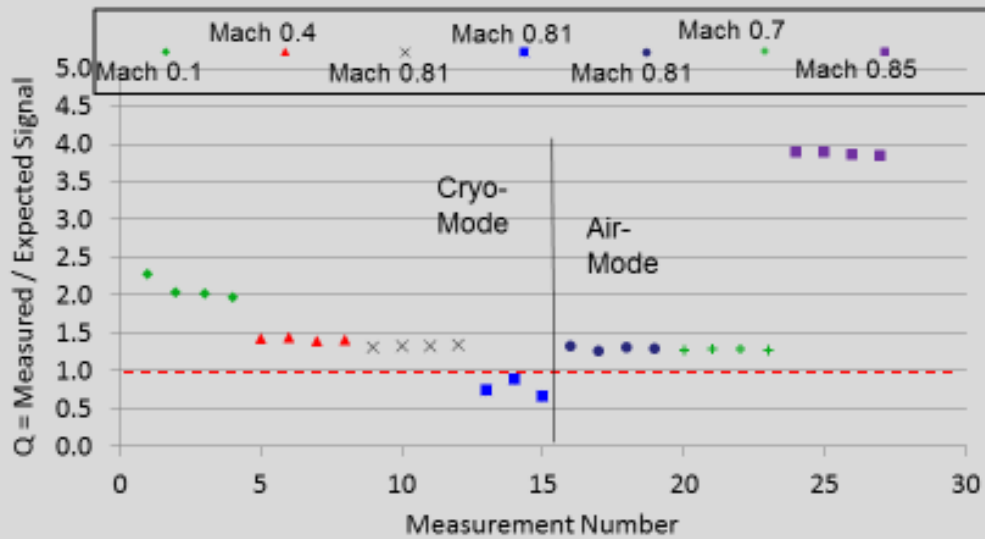
Figure 3c. Example of 27 points (each a 10-image average) for Q for seven different run
conditions, three in air-mode and four in cryo-mode. The dashed red line
indicates Q = 1, where the measurements agree with the calculated
expectation. The results generally indicate no clustering.
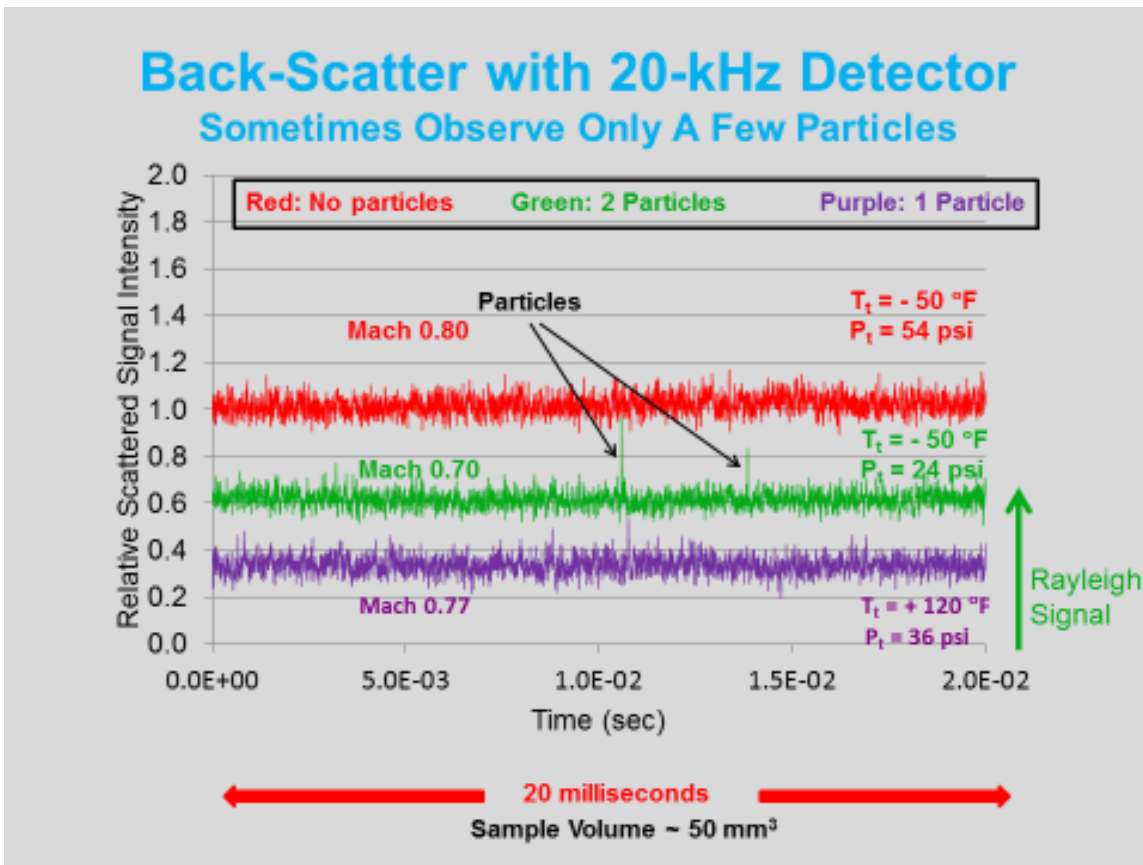
Figure 4. Three examples of 20-ms windows of RLS back-scatter signal on the PMT for three run conditions (two cryo-mode and one air-mode) showing occasional particles.
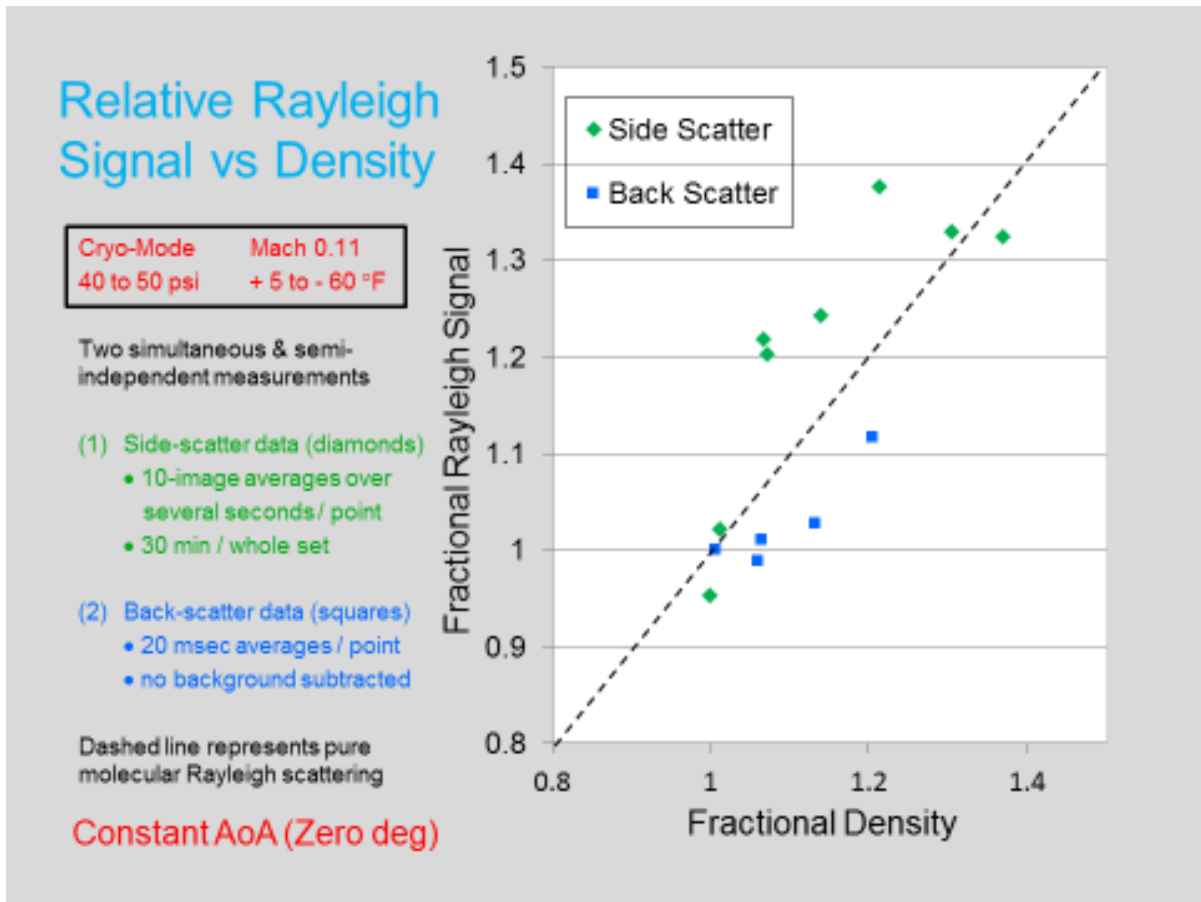
Figure 5. Near simultaneous back and side-scatter fractional signals versus fractional flow density ρ_s. Data are consistent with a linear relationship with unity slope to within about $\pm 10\%$.
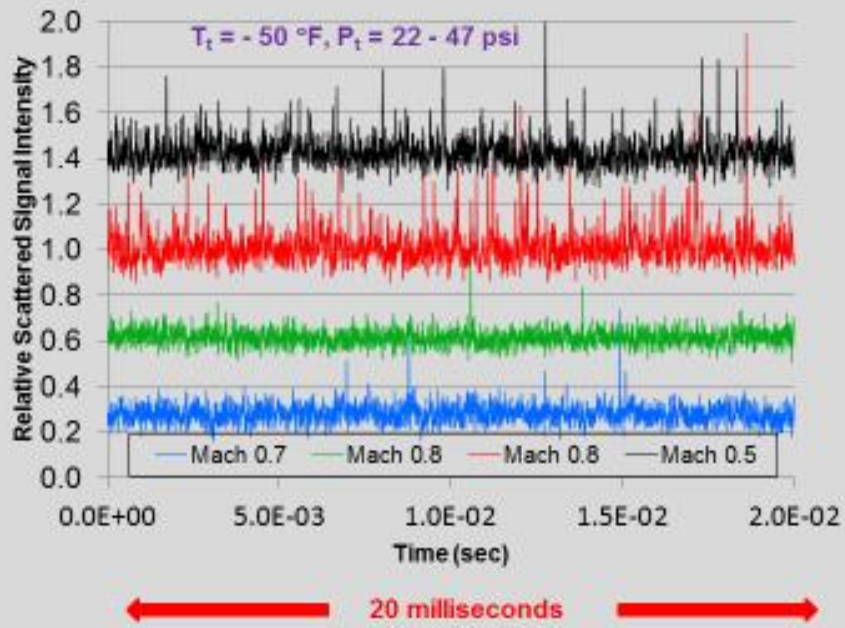
Figure 6. Four examples of RLS backscatter, two (green and blue) with a smaller particle flux [~ 1 particle/(mm^2 sec)] and two (red and black) with much larger particle flux [~ 20 particles/(mm^2 sec)].

Cryo-Mode Side-Scatter Results

Temperature = - 37 °F	T_t = - 50 °F
Flow Off	Mach 0.7
High Particle Density	3 Particles / 20 msec

2150-0000   Exposure time ≈ 20 msec   2153-0006

Figure 7. Flow-on (right side with three particles denoted by red arrows) and flow-off (left side with many particles) 20-ms images of laser beam in cryo-mode.

Air-Mode Side-Scatter Results

Temperature ≈ + 37 ℉ T_t = - 120 ℉
Flow Off   Mach 0.4
Low Particle Density   No Particles / 20 msec
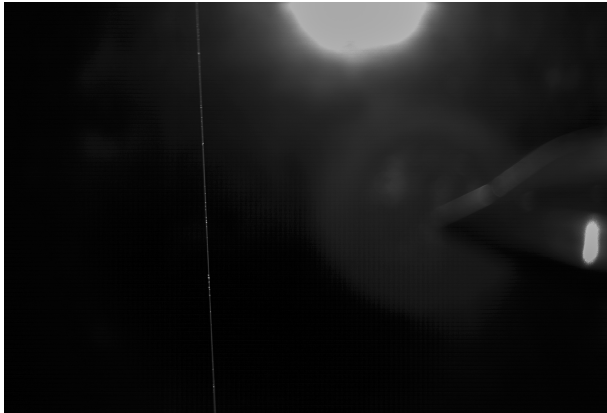
2552-0000   2570-0000

Reduced field of view
for this image

Figure 8. Flow-on (right-side with no particles and reduced FOV) and flow-off
(left-side with many particles and standard FOV as in Figures 2 and 7)
20-ms images of laser beam in air-mode.
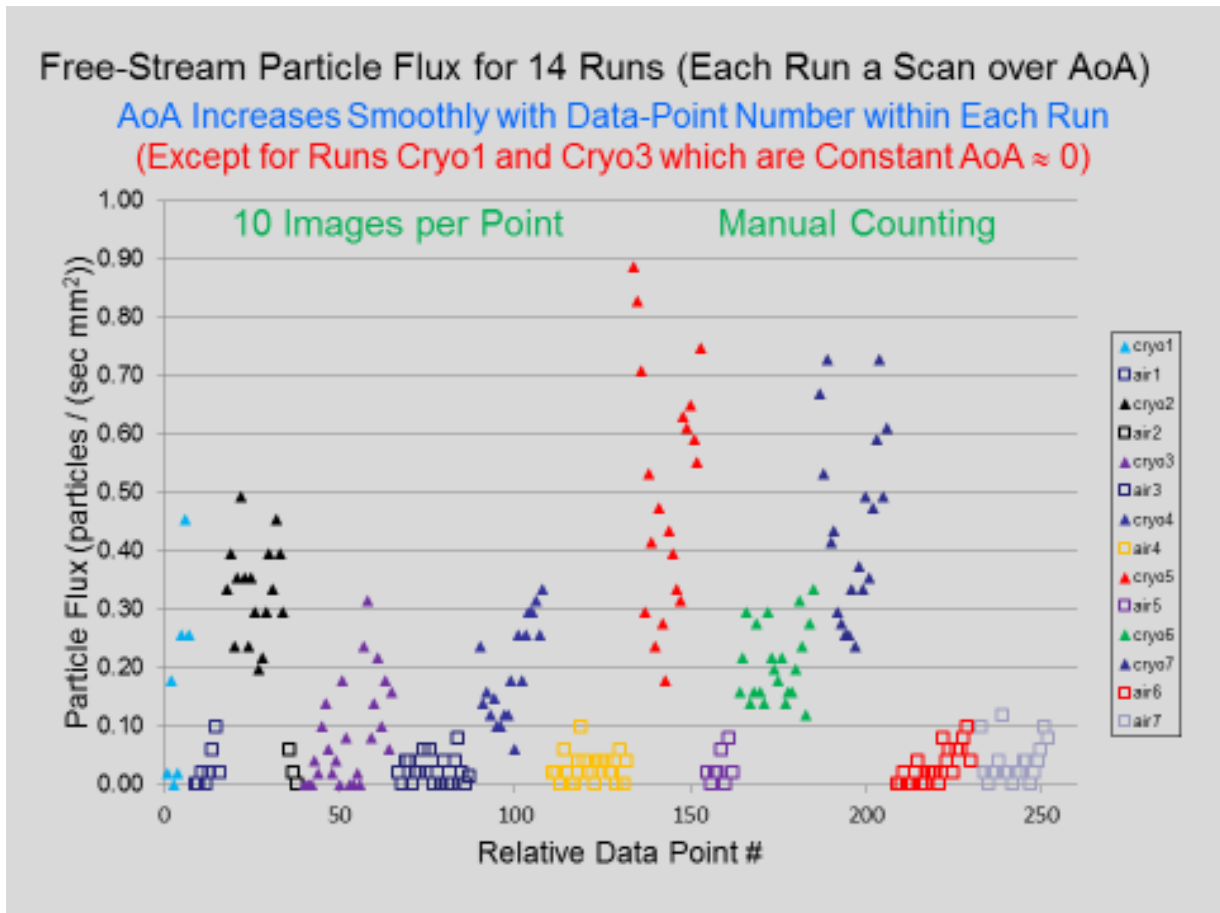
Figure 9. Particle flux for ~ 150 test points (each an average over 10 images) over 7 cryo and 7 air-mode run conditions. Cryo-mode shows ~ 10 times larger flux than air-mode for the GCH manual counts shown here. For automated counting (see particle flux estimates from Figure 13) the cryo-mode counts are ~ 30 to 100 times the air-mode counts shown here.
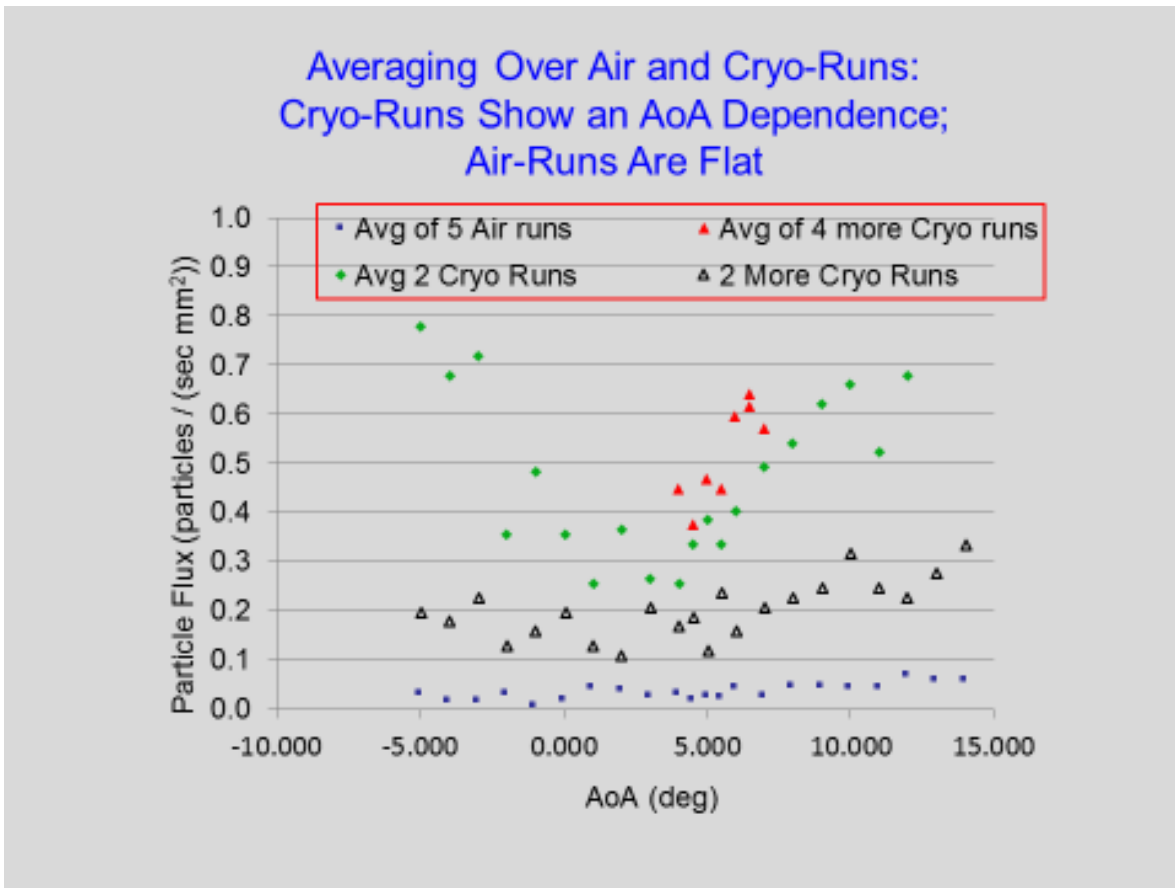
Figure 10. Particle flux averages versus AoA for cryo and air-mode conditions. Each run is one scan over AoA. Red filled triangles show an average of 4 cryo-runs, green diamonds show an average of two different cryo-runs, black open triangles show an average of two additional cryo-runs, and blue squares show an average of five air-runs. Cryo-mode averages shows AoA dependence, while air-mode runs are approximately flat with AoA.
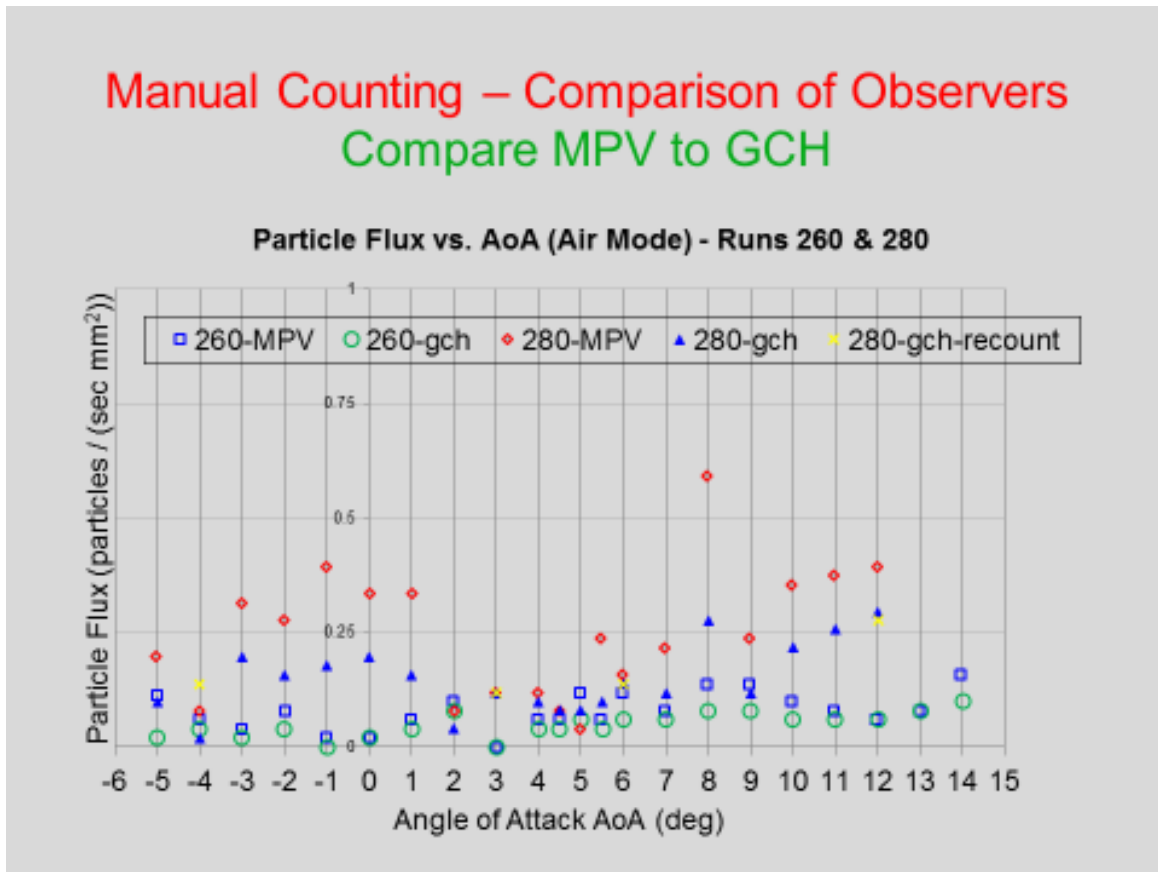
Figure 11: Comparison of manual particle counting results with two runs (260 and 280) and two observers (GCH & MPV). GCH originally spent less time per image than MPV. For GCH's Run 280 <u>recount</u>, GCH purposefully spent more time, found more particles relative to GCH's first quicker count. The values for the GCH recount are in agreement with MPV. Thus the two observers found similar particle fluxes when GCH started spending more time (similar to the times spent by MPV) looking for particles.
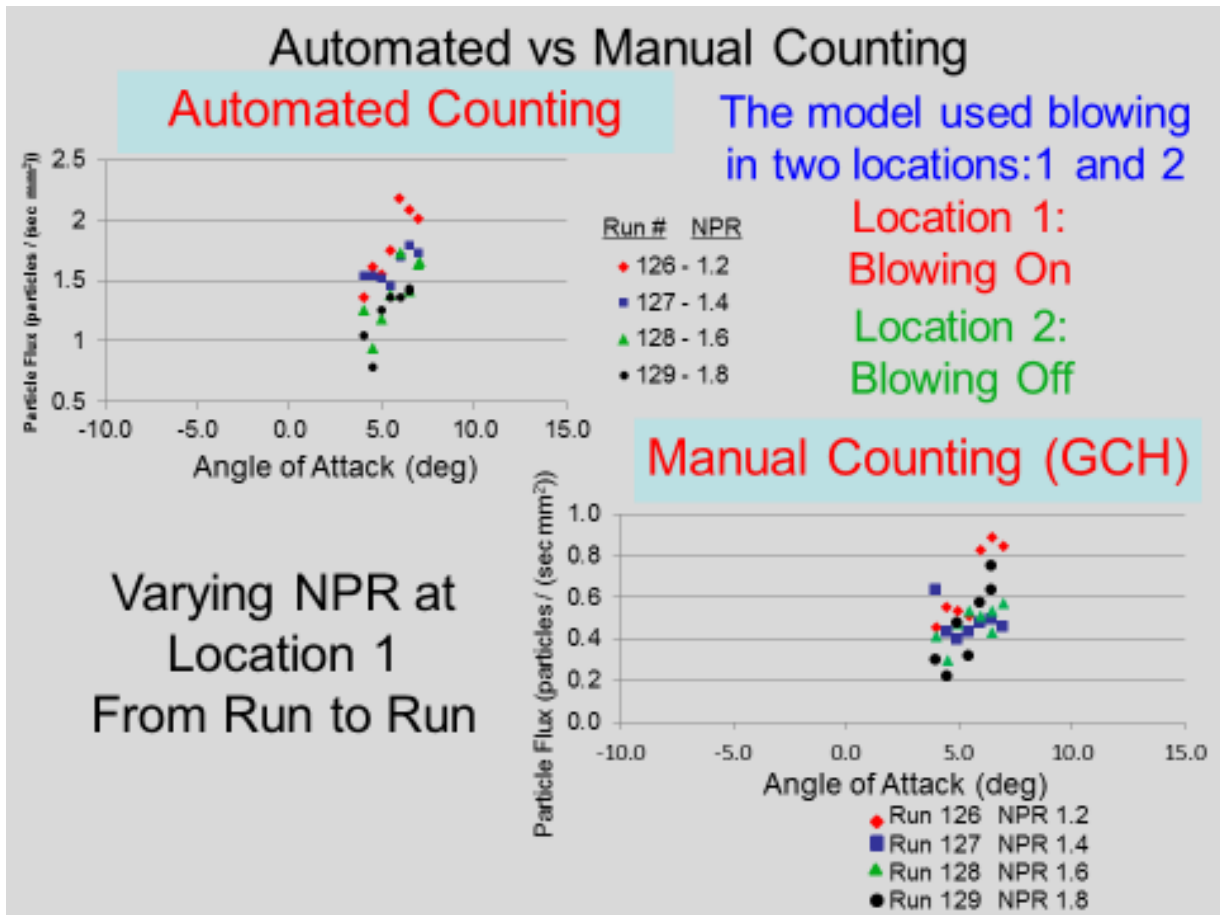
Figure 12. Comparison of manual and automated particle counting for four runs. Inspection of the two vertical scales reveals that automated counting typically finds twice as many particles as manual counting by observer GCH. A second observer MPV typically found twice as many particles as GCH's original quick searches for particles shown here. After GCH spent more time searching for particles, the GCH counts approximately doubled and then the manual counts by GCH and MPV and the automated counts were all in general agreement.
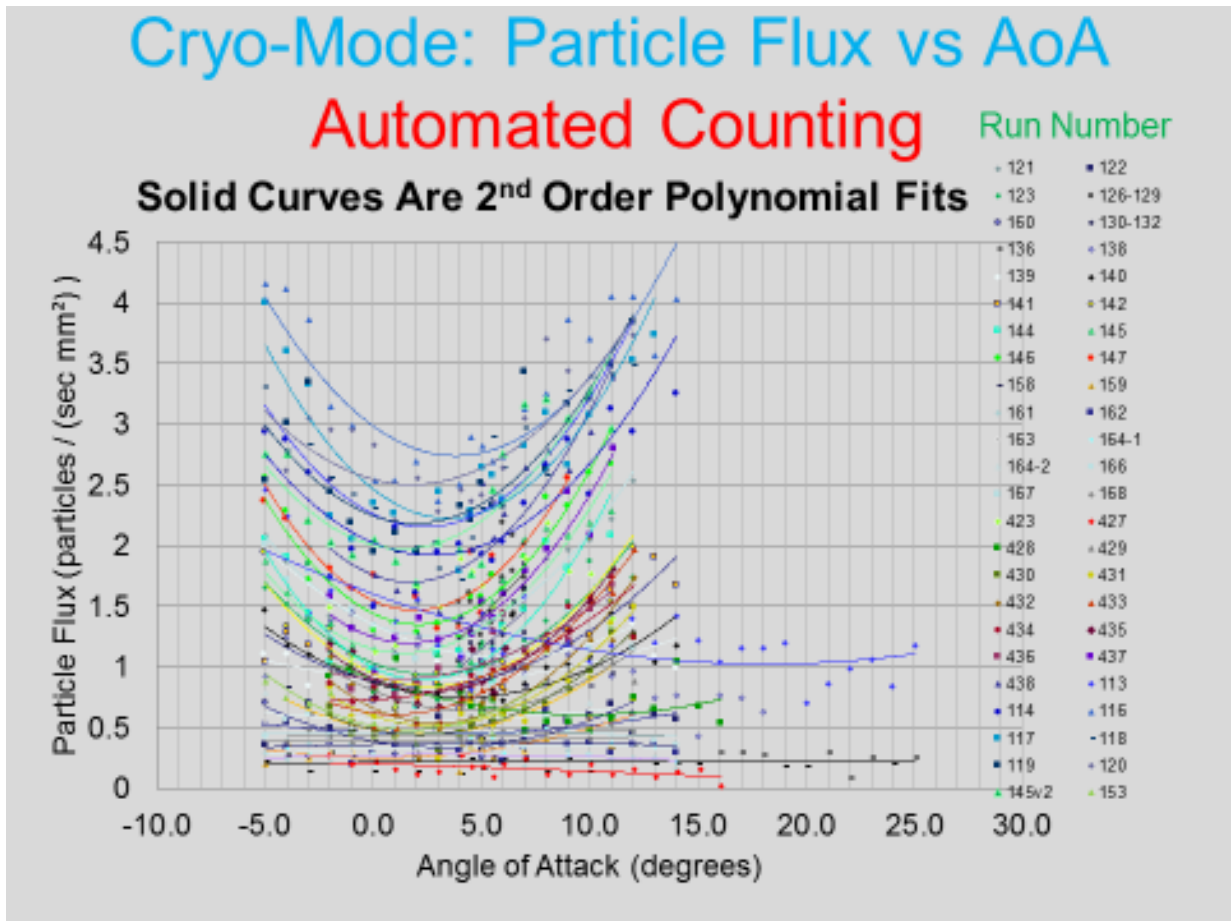
Figure 13. Particle flux versus AoA by automated counting for about 50 cryo-mode runs. Solid curves are fits to Equation 4 for each run.
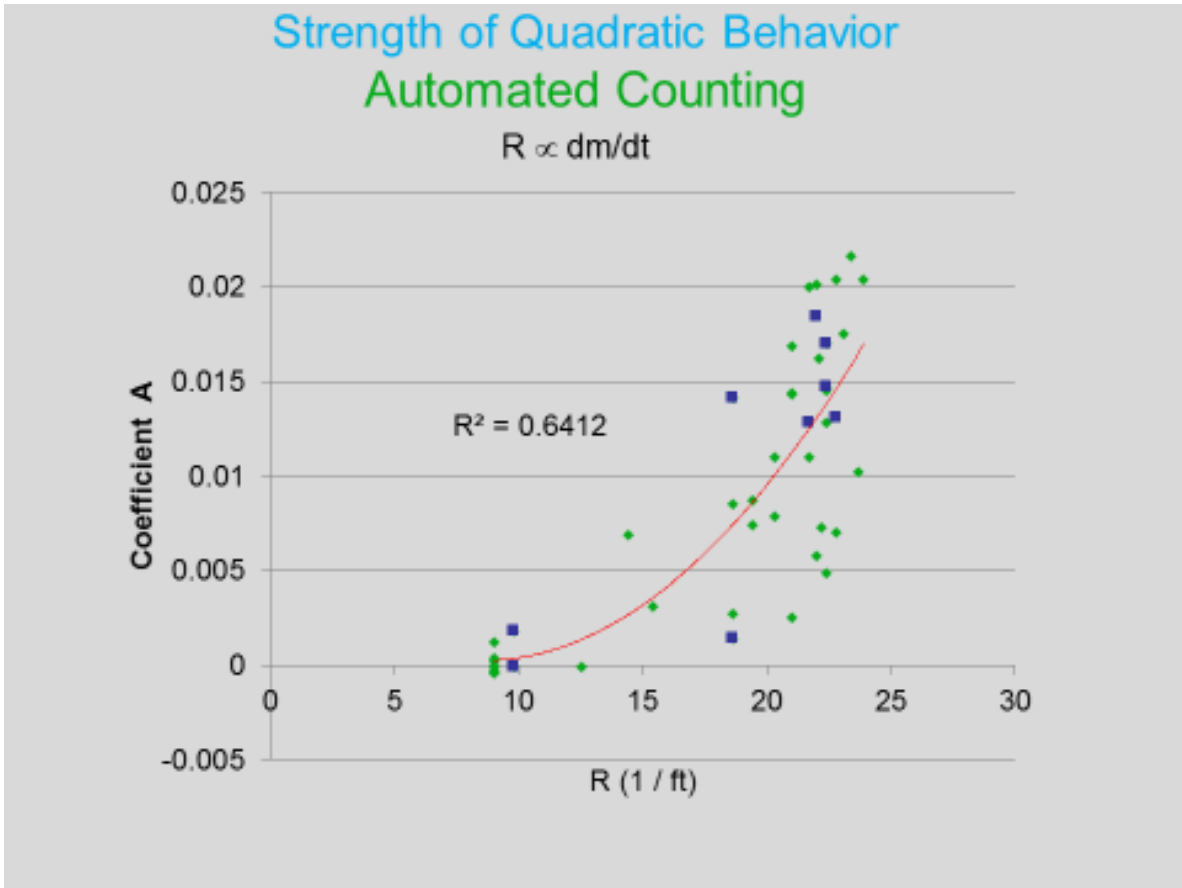
Figure 14. Fitted constant A, from Equation 4, plotted versus R. Larger A values indicate more quadratic behavior if plotting particle flux versus AoA. This data shows that the AoA quadratic behavior of Figure 13 is not strongly correlated to R (or mass flow).
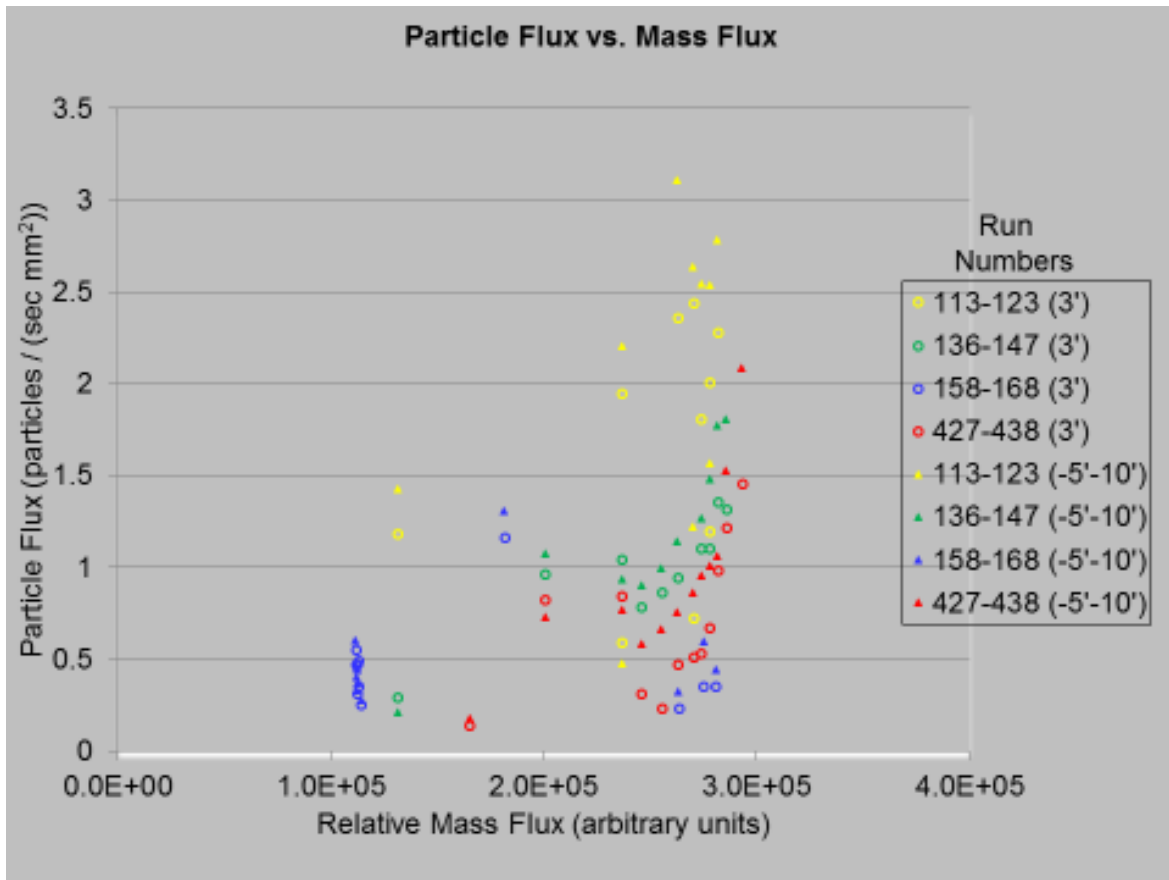
Figure 15. Data from Figure 14 plotted versus mass flux down the test section, showing the same poor correlation result as in Figure 14. Open points are for 3 deg AoA only; filled points are for averaging over -5 to + 10 deg AoA.
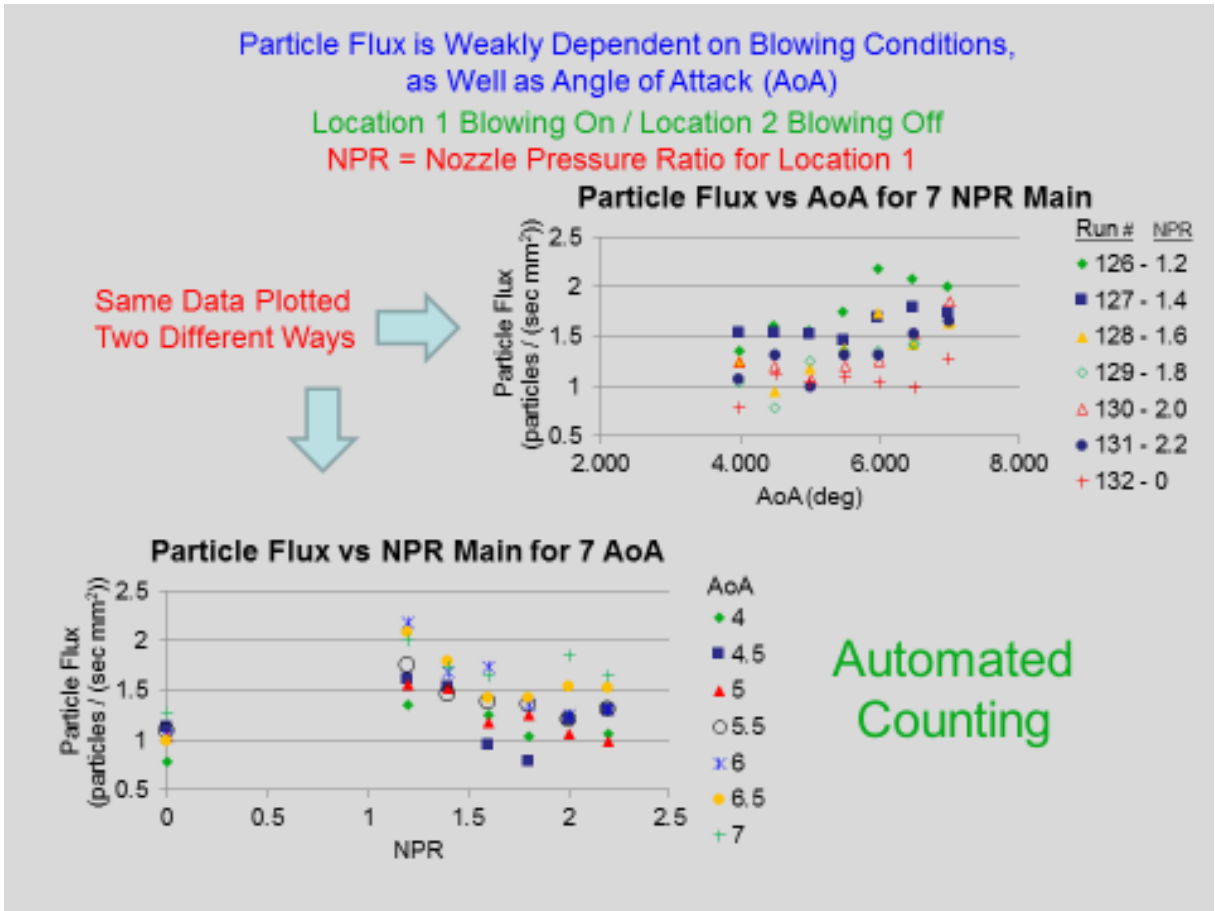
Figure 16. Two different plots of the same data for particle flux from seven cryo-mode runs with varying NPR. The top plot shows particles versus AoA for seven NPR and the bottom plat shows particles versus NPR for seven AoA. NPR = 0 indicates no blowing and does not mean that tunnel fluid is being sucked into the model; this data is arbitrarily plotted at NPR = 0 instead of NPR = 1 to remind the reader that this is a no blowing condition.
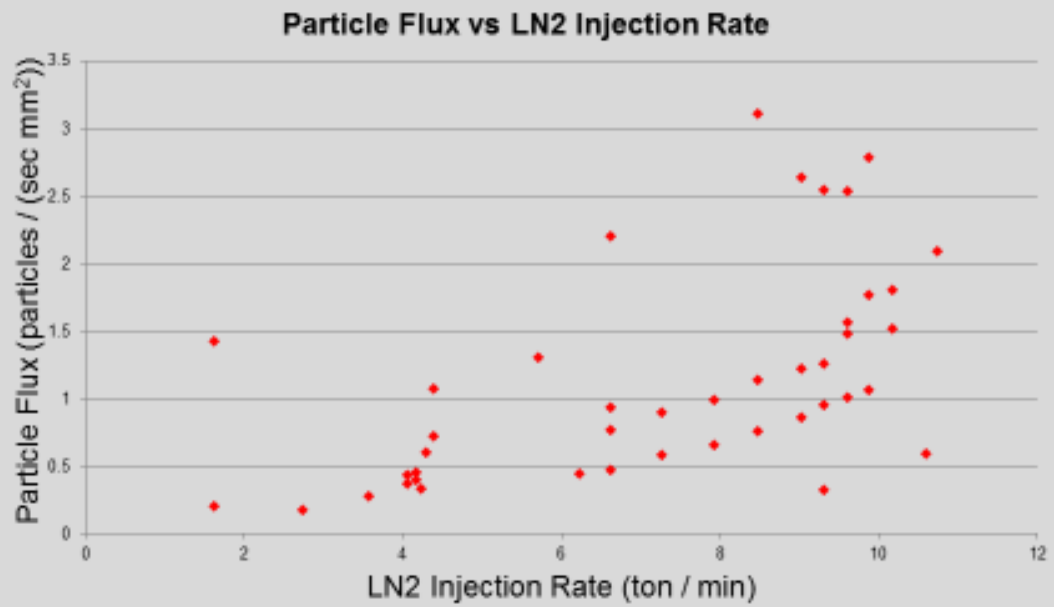
Figure 17. Particle flux data (same runs as in Figure 13) averaged over AoA versus rate
of liquid N_2 injection rate.
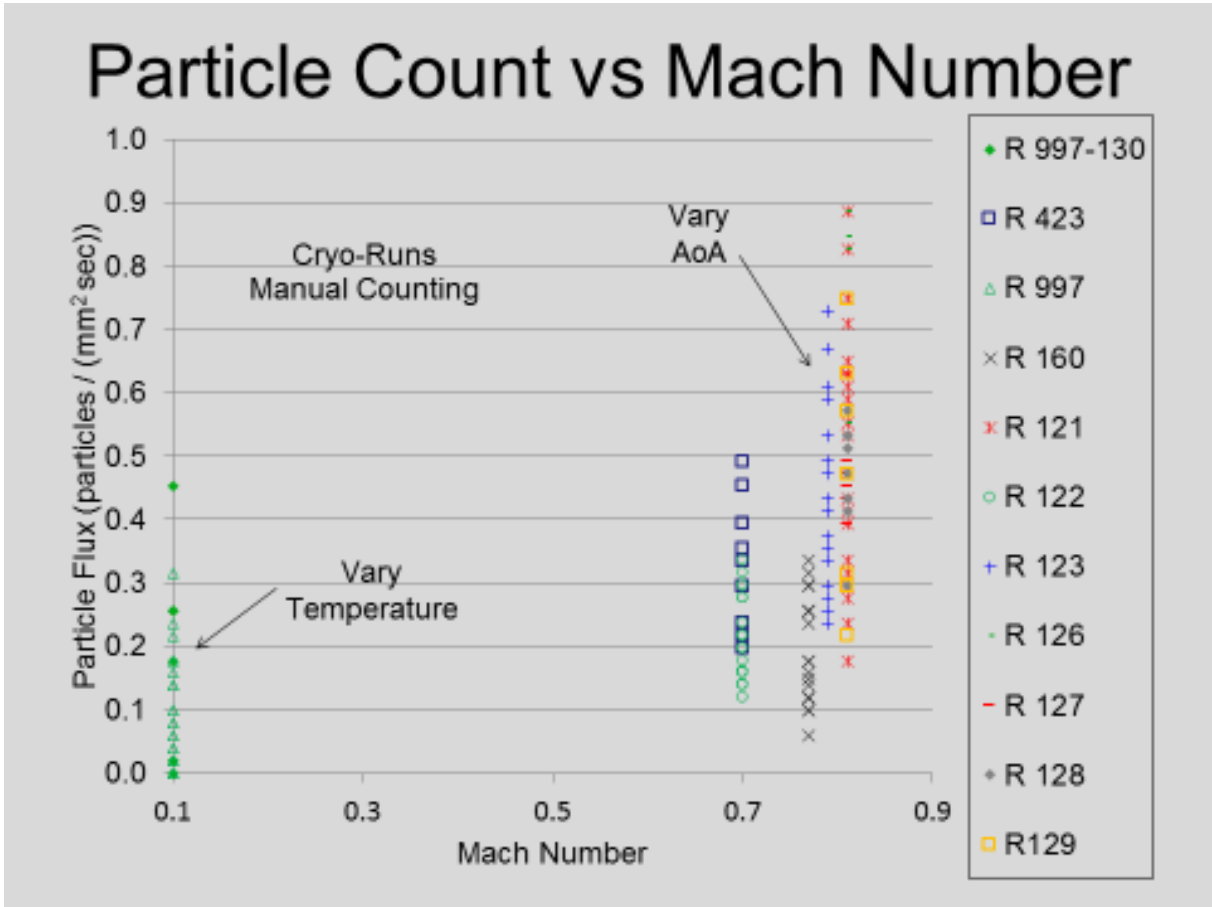
Figure 18. Particle flux versus M (vertical range of the data is due to cooling the flow at constant AoA (Mach 0.1) and due to varying AoA at constant T_t (Mach 0.7 – 0.8).
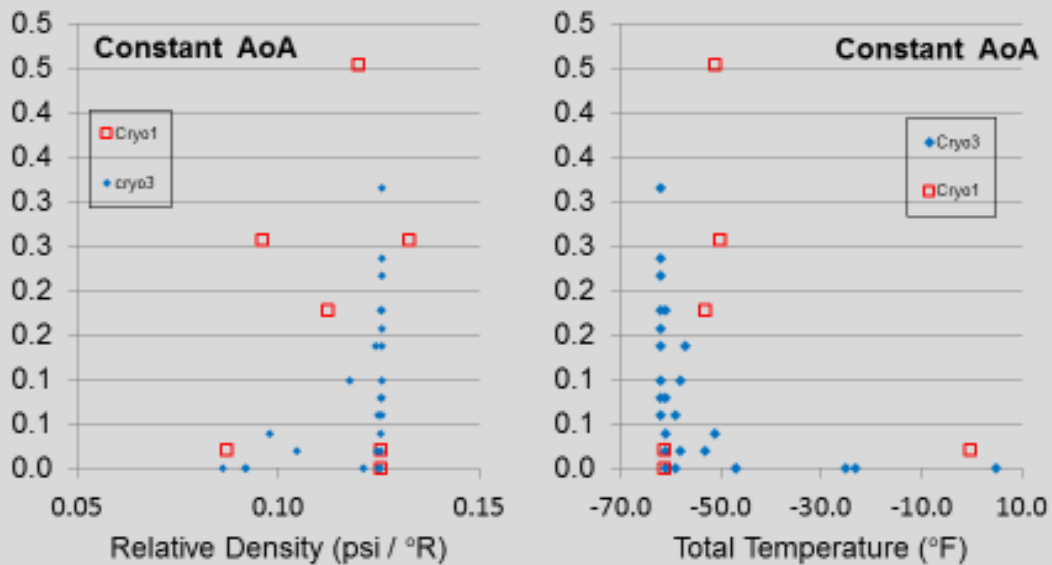
Figure 19. Two plots of the same particle flux data for two different cryo-runs (red boxes and blue filled diamonds) with constant AoA and a large variation of T_t: versus relative total density = P_t / T_t on the left and versus T_t on the right. Note the different units for the two plots and the unusual units for the horizontal scale for the left-hand plot.
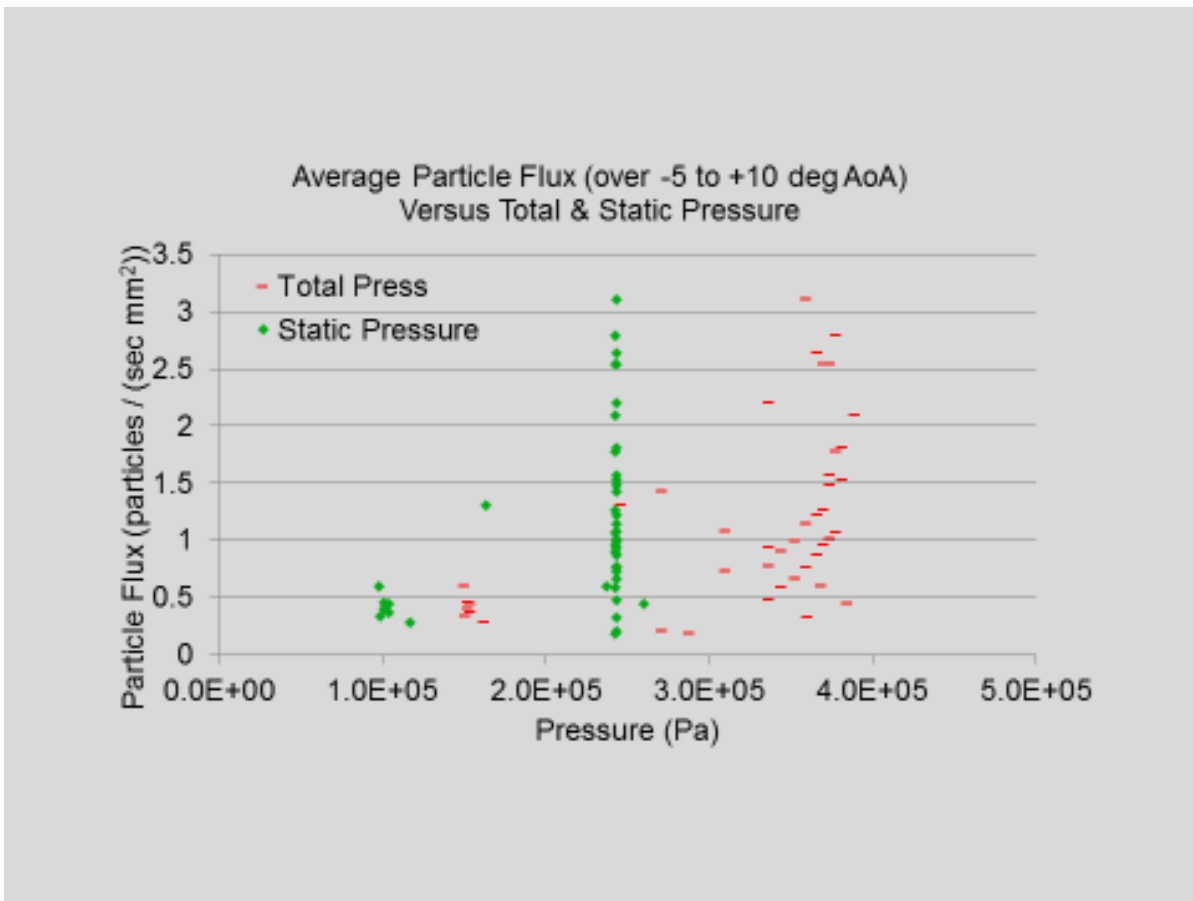
Figure 20. Particle flux for 42 runs (each run a scan over AoA averaged over the entire run and hence AoA) and plotted twice: versus P_t (red bars) and P_s (green diamonds).
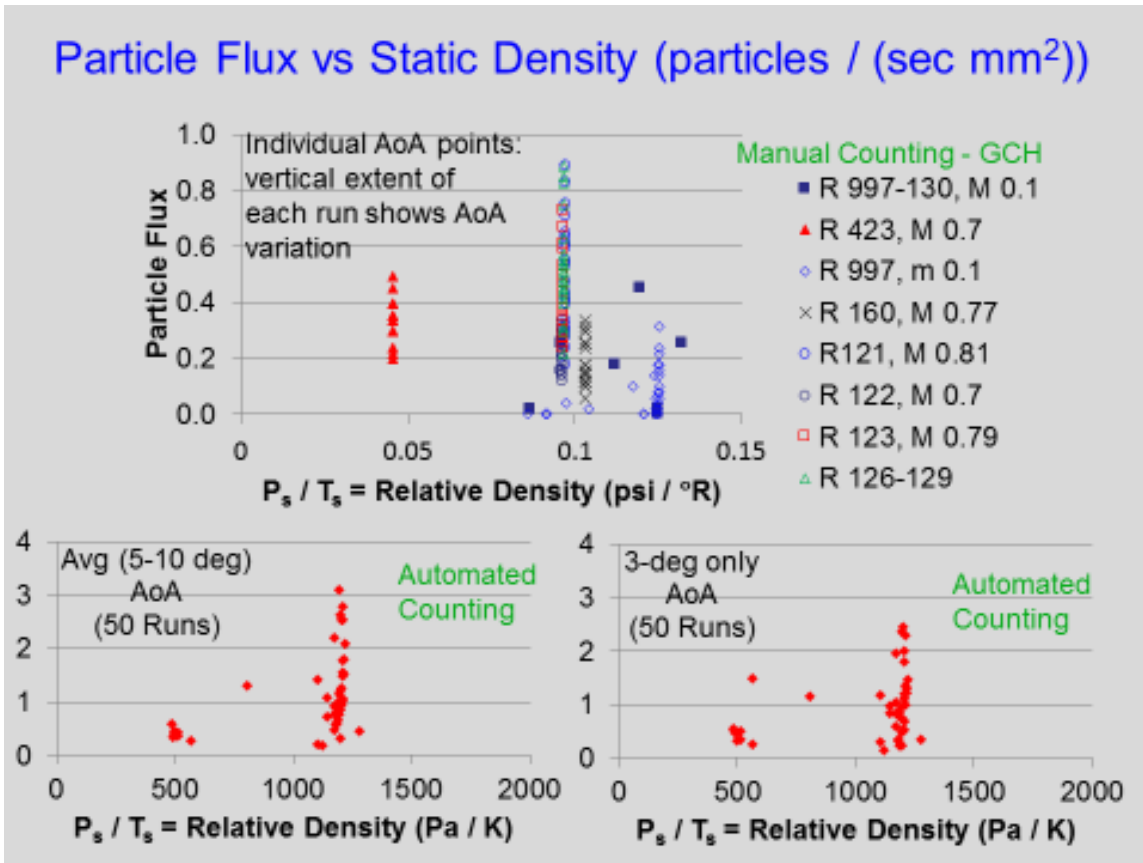
Figure 21. Particle flux plotted in three ways versus ρ_s. In the top plot, each point is constant AoA; Mach number for each run is indicated in the legend. In the lower left plot, each point is averaged over AoA from + 5 to +10 deg. In the lower right plot, each point is for AoA = 3 deg. Note that the different units for the horizontal scales of the top and lower plots and that these unusual units are for relative static density (not absolute). The top plot is manually counted, while the lower plots use automated counting. Particle flux is not strongly correlated to ρ_s for both 3 deg AoA and averages over AoA.
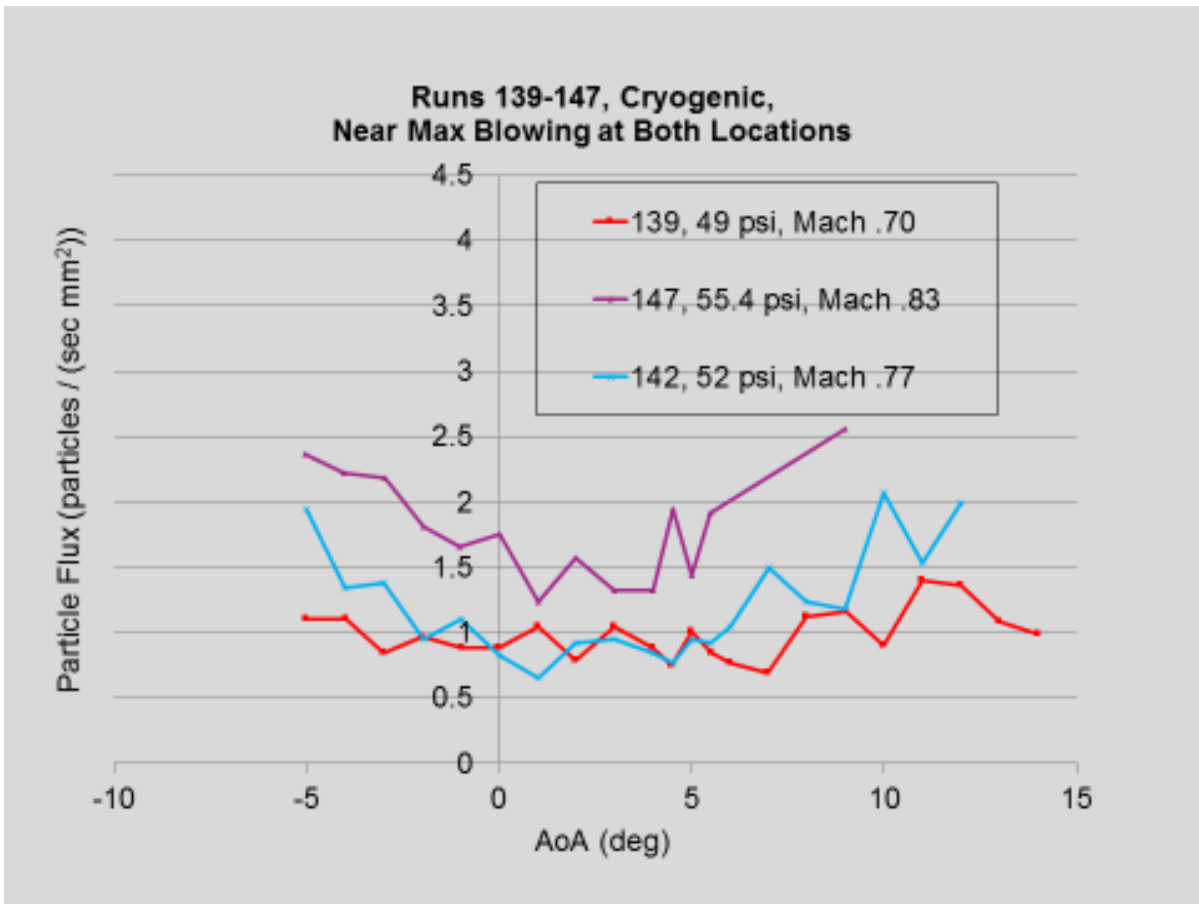
Figure 22a. Three runs (147, 142, and 139, each a scan over AoA) for conditions listed in legend. Larger M (i.e. colder) and larger P_t generally produce more particles at almost all AoA.
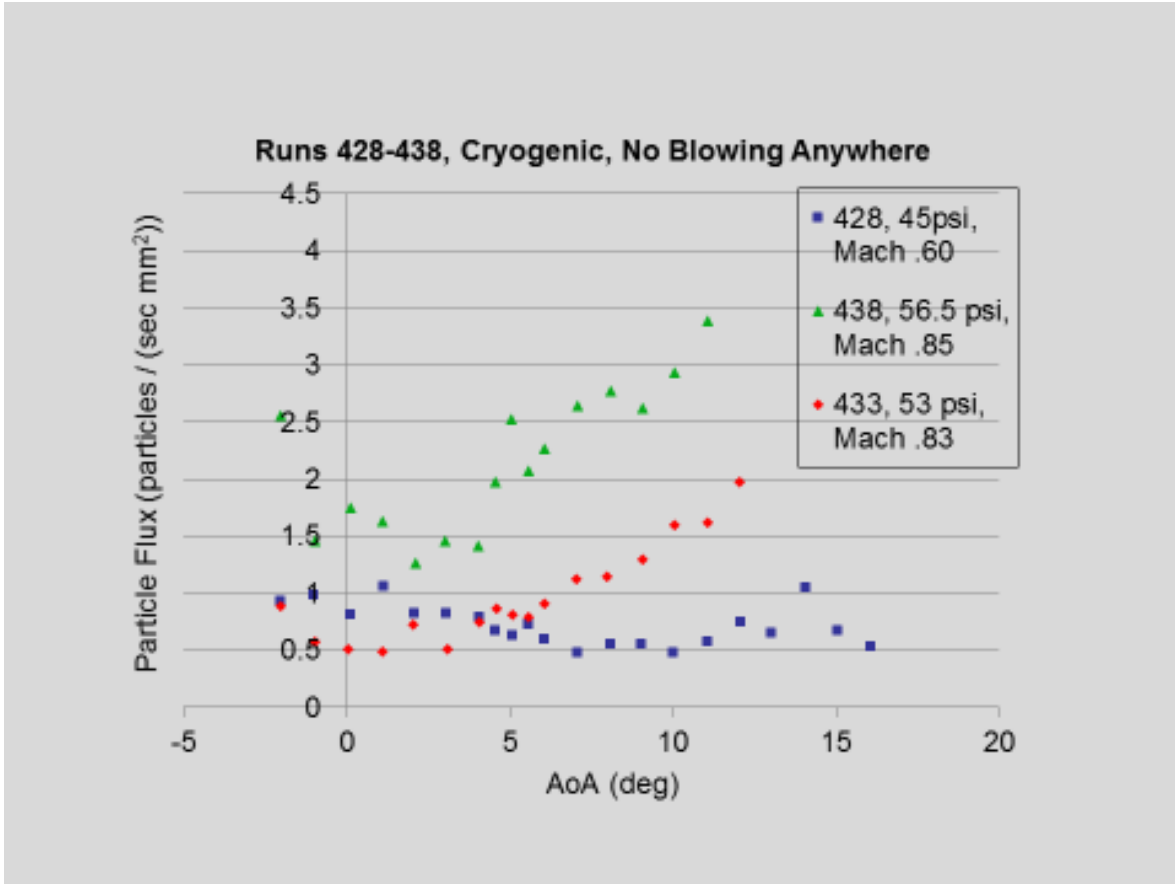
Figure 22b. Three runs (each run a scan over AoA) for conditions listed in legend. Larger M (i.e. colder) and larger P_t generally produce more particles at almost all AoA.
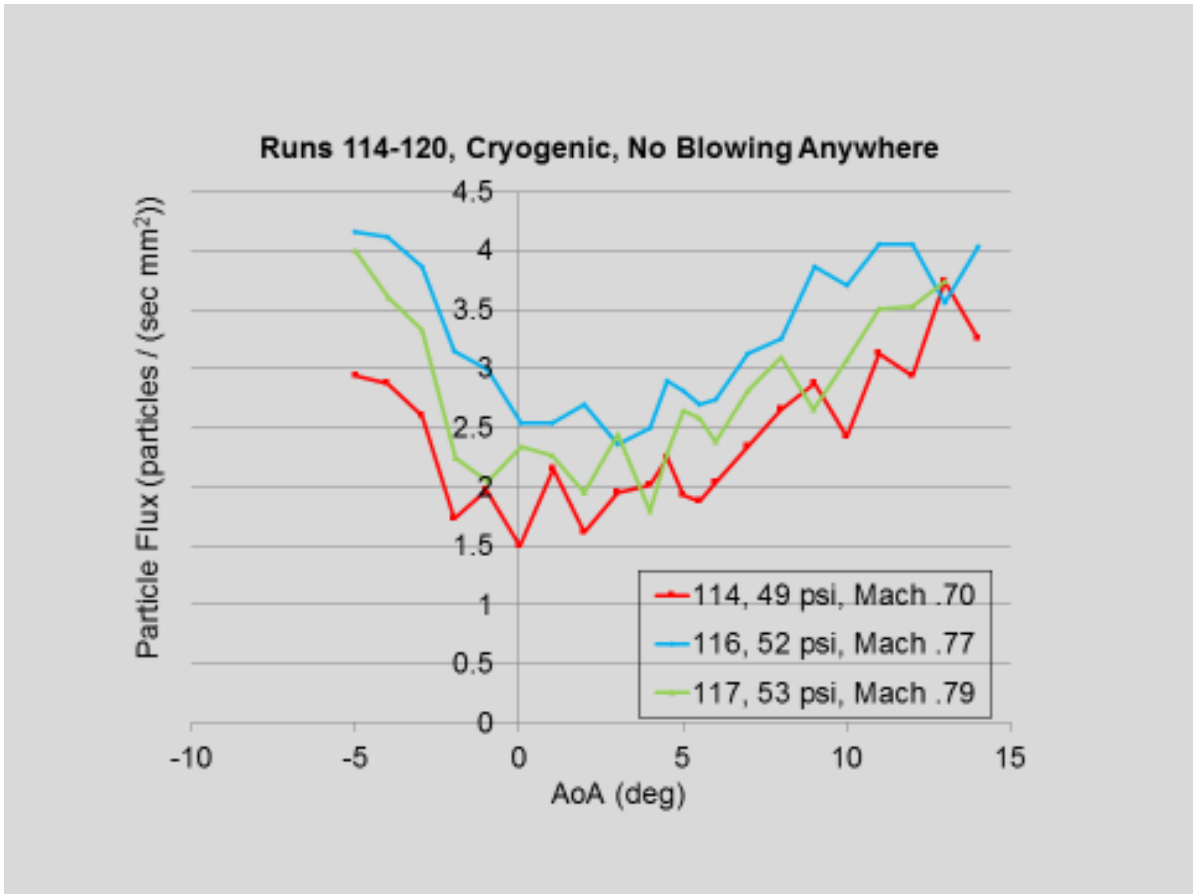
Figure 22c. Three runs for conditions listed in legend. Larger M (i.e. colder) and larger P_t generally produce more particles with exception of green curve at Mach 0.79.
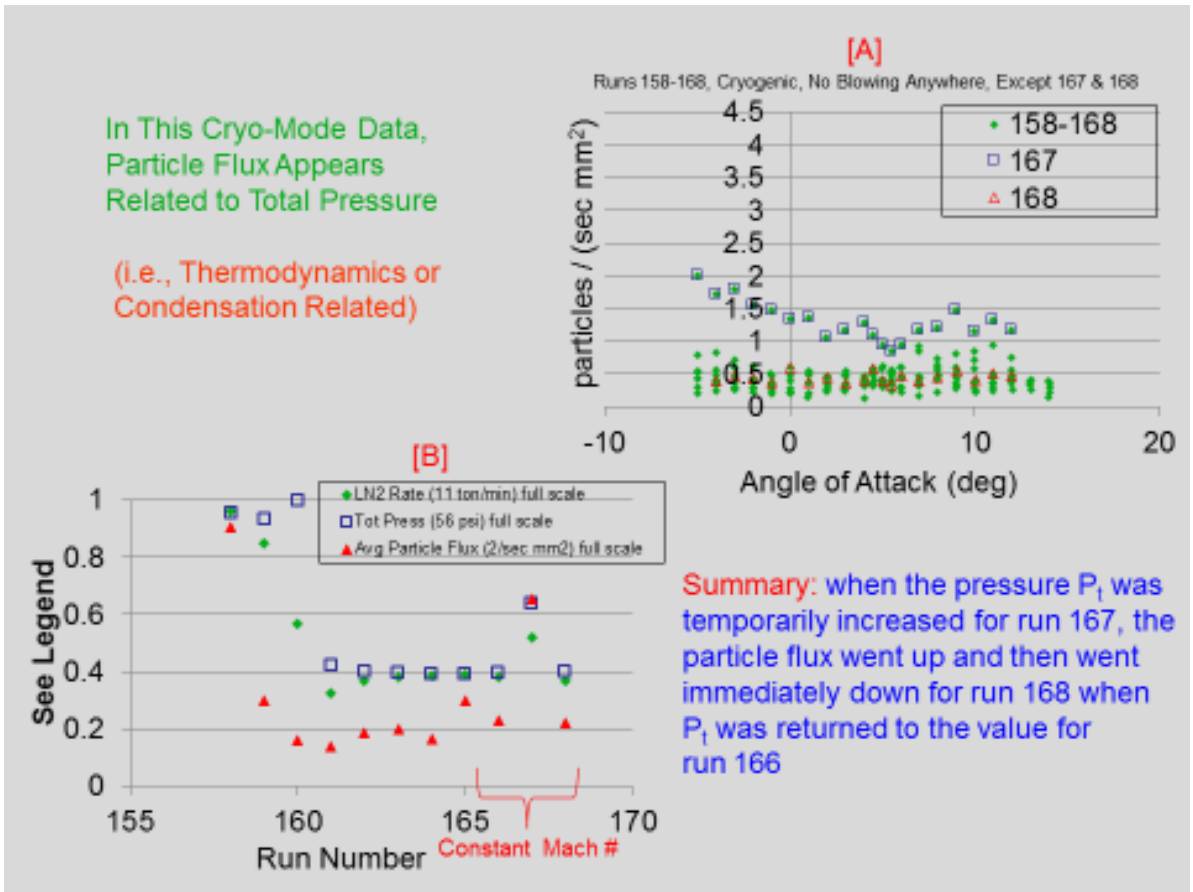
Figure 23. Two ways ([A] top and [B] bottom) of plotting eleven consecutive runs (each run a scan over AoA) for constant conditions at $P_t = 22$ psi, except run 167 (denoted by blue boxes in [A]) has P_t increased from 22 to 35 psi. In [A] each scan versus AoA is shown. In [B] each run over AoA is averaged into one point and plotted versus run number as solid red triangles. LN2 injection rate (green triangles) and P_t (blue boxes) are also shown in [B}], so all plots are relative and the units for each curve are shown in the legend. Although this instance of temporary pressure increase was limited during the test, this example shows evidence for a small but clear increased particle flux for larger P_t (or possibly LN2 injection rate).
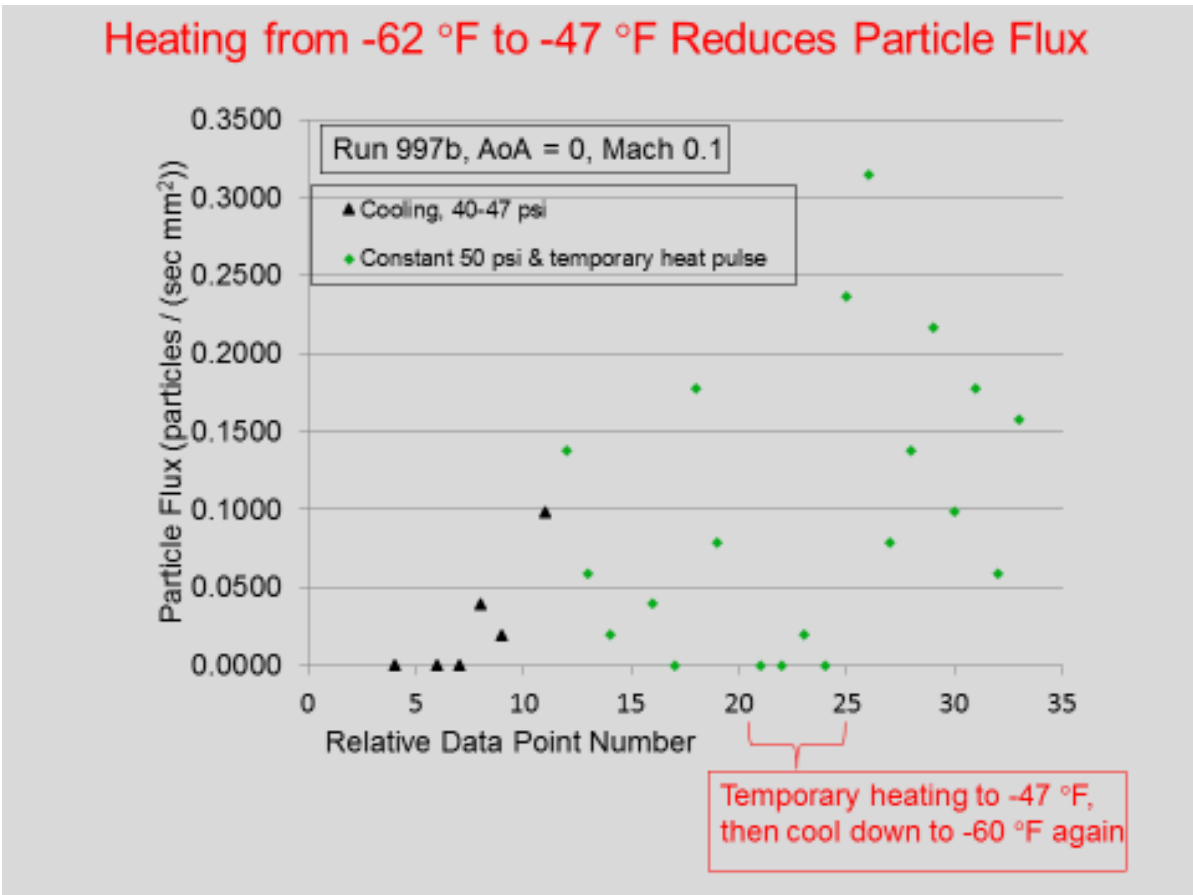
Figure 24. Particle flux versus consecutive test point number over 2.5 hours. Black triangles show data while the tunnel is still cooling down. Green diamonds show data after the tunnel has reached the T_t = -62 deg F set point. For points 21-24 the flow was temporarily heated from -62 °F to -47 °F, followed by a return to -62 °F at run 25. This type of temporary slight heating of the flow was limited, and this example shows a particle flux dependence on T_t.
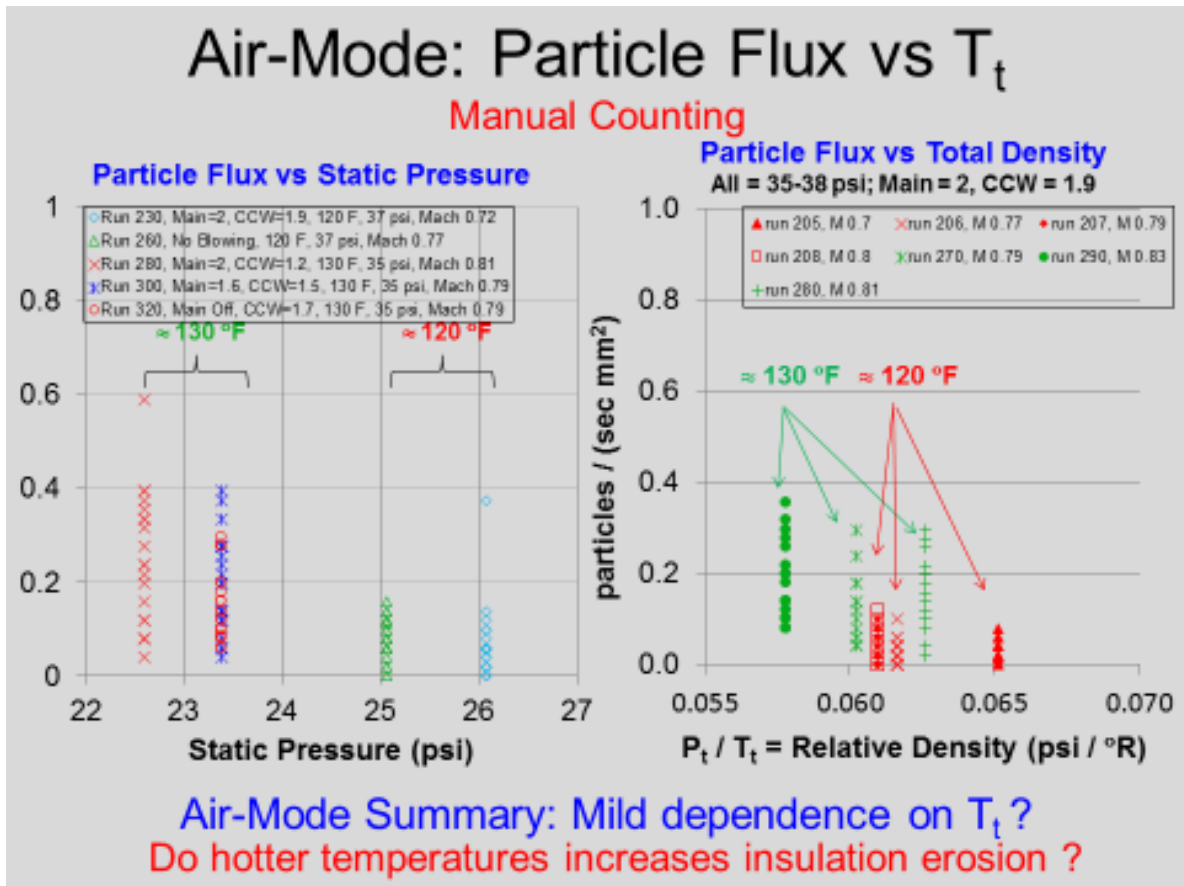
Figure 25. Synopsis of 12 air-mode runs for constant P_t of $\approx$ 35 psi, each run a scan over AoA. On average, T_t = 130 °F appears to generate slightly more particle flux than T_t = 120 °F. Note the unusual units on horizontal axis of the right-hand plot.
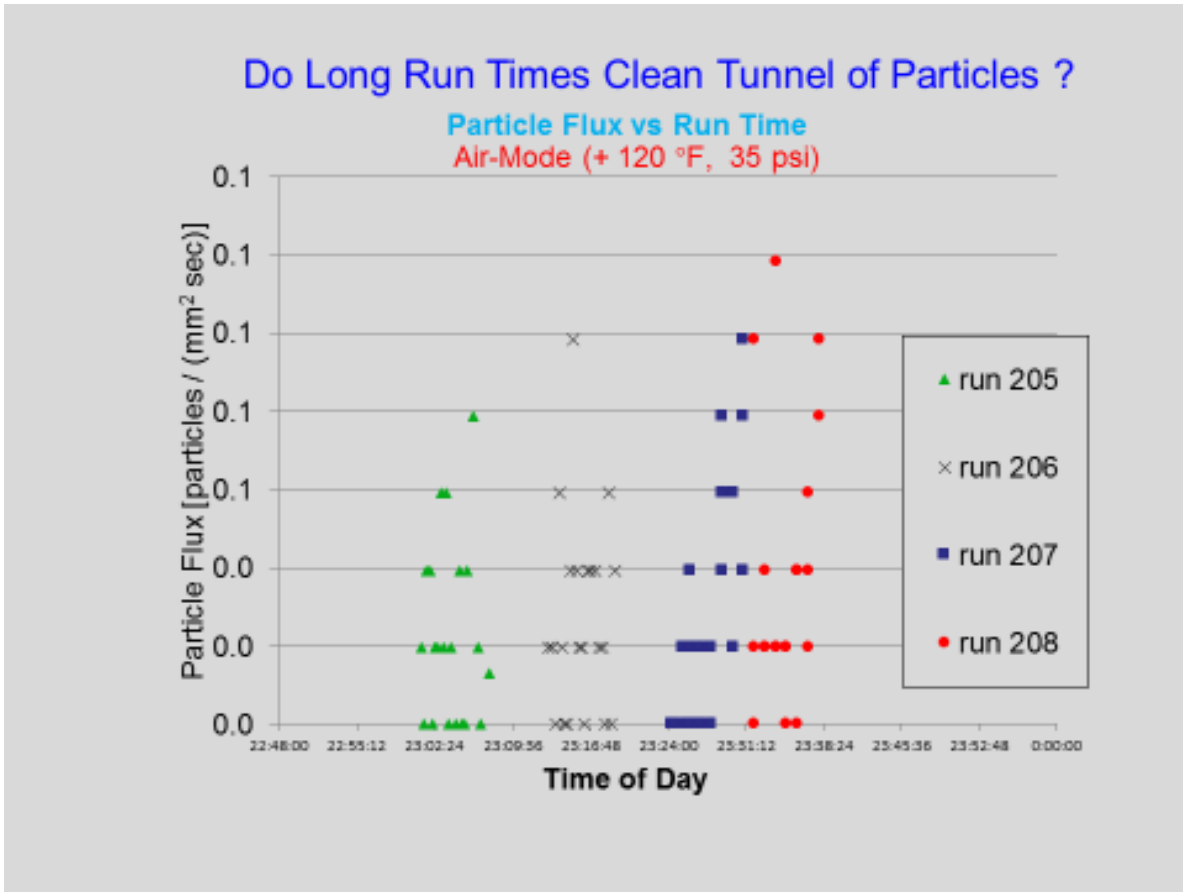
Figure 26. Particle flux variation versus time-of-day for four air-mode runs, each run a scan over AoA (thus each point is a different AoA). There is no observed particle flux decrease with increased runtime in air-mode.
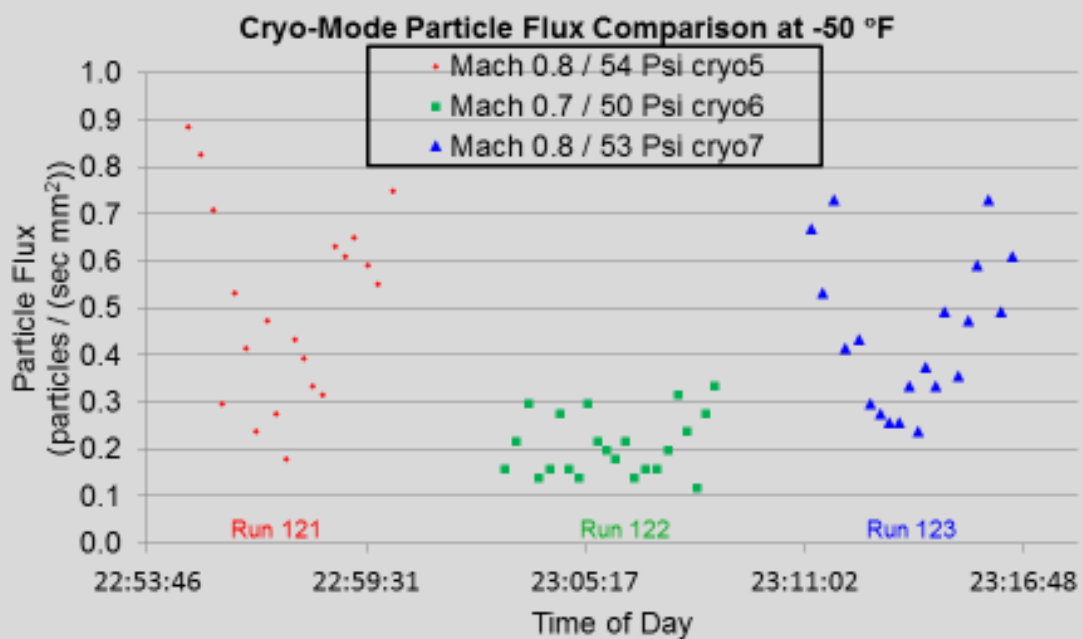
Figure 27. Particle flux versus time for three successive runs, each a scan over AoA (thus each point is a different AoA). This AoA variation with time generates the characteristic "u" shape with time. There is no sign of cleaning over two continuous hours of running in cryo-mode.
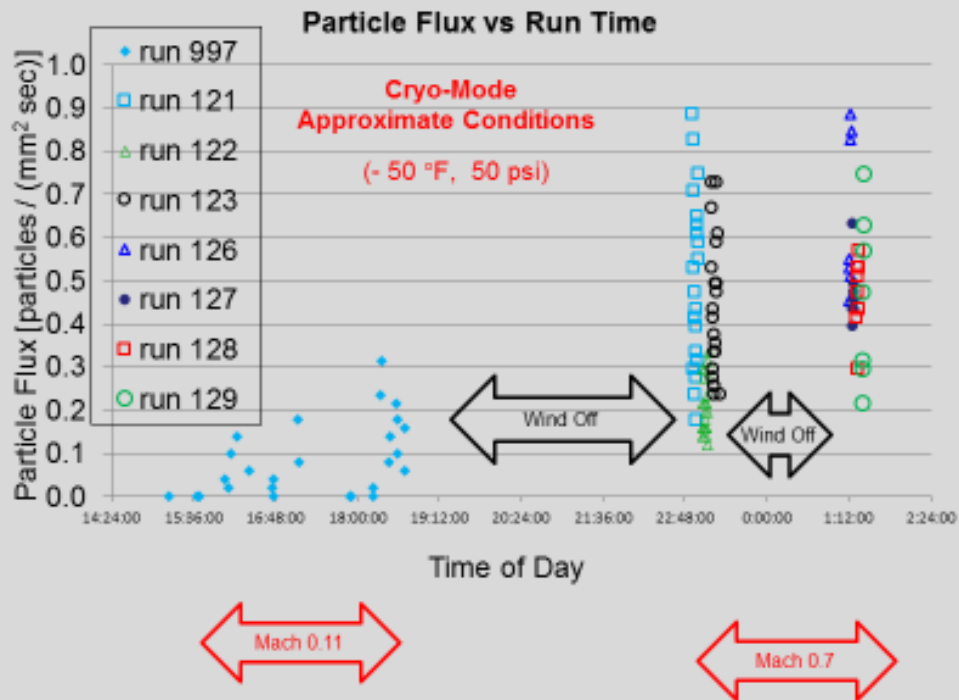
Figure 28. Particle flux versus time of day with wind-off periods noted. The apparent increase with Mach number is probably not real or important for this data set, because P_t and T_t are also changing over this data set. There is no observed flux decrease with increased runtime over the course of a day.

REPORT DOCUMENTATION PAGE

1. REPORT DATE *(DD-MM-YYYY)*	2. REPORT TYPE	3. DATES COVERED *(From - To)*
01-09-2015	Technical Memorandum	

4. TITLE AND SUBTITLE

Feasibility of Rayleigh Scattering Flow Diagnostics in the National Transonic Facility

5a. CONTRACT NUMBER

5b. GRANT NUMBER

5c. PROGRAM ELEMENT NUMBER

6. AUTHOR(S)

Herring, Gregory C.; Lee, Joseph W.; Goad, William K.

5d. PROJECT NUMBER

5e. TASK NUMBER

5f. WORK UNIT NUMBER

147016.03.07.01.05.03

7. PERFORMING ORGANIZATION NAME(S) AND ADDRESS(ES)

NASA Langley Research Center
Hampton, VA 23681-2199

8. PERFORMING ORGANIZATION REPORT NUMBER

L-20599

9. SPONSORING/MONITORING AGENCY NAME(S) AND ADDRESS(ES)

National Aeronautics and Space Administration
Washington, DC 20546-0001

10. SPONSOR/MONITOR'S ACRONYM(S)

NASA

11. SPONSOR/MONITOR'S REPORT NUMBER(S)

NASA-TM-2015-218800

12. DISTRIBUTION/AVAILABILITY STATEMENT

Unclassified - Unlimited
Subject Category 74
Availability: NASA STI Program (757) 864-9658

13. SUPPLEMENTARY NOTES

14. ABSTRACT

Laser-based Rayleigh light scattering (RLS) was performed in the National Transonic Facility (NTF) at NASA Langley Research Center. The goal was to determine if the free-stream flow undergoes clustering (early stage of condensation from gas to liquid) or remains in a pure diatomic molecular phase. Data indicate that clusters are not observable down to levels of 10% of the total light scatter for a variety of total pressures at one N2 cryogenic-mode total temperature (Tt = -50 degF = 227 K) andone air-mode temperature (Tt = +130 degF = 327 K). Thus RLS appears viable as a qualitative or quantitative diagnostic for flow density in NTF in the future.

15. SUBJECT TERMS

Condensation; Cryogenic wind tunnel; Molecular clusters; National Transonic Facility; Particles; Rayleigh Light Scattering

16. SECURITY CLASSIFICATION OF:			17. LIMITATION OF ABSTRACT	18. NUMBER OF PAGES	19a. NAME OF RESPONSIBLE PERSON
a. REPORT	b. ABSTRACT	c. THIS PAGE			STI Help Desk (email: help@sti.nasa.gov)
U	U	U	UU	59	19b. TELEPHONE NUMBER *(Include area code)* (757) 864-9658